EARTH SURFACE PROCESSES AND LANDFORMS
Earth Surf. Process. Landforms **43**, 2698–2714 (2018)

Published online 7 August 2018 in Wiley Online Library
(wileyonlinelibrary.com) DOI: 10.1002/esp.4425

Variations in near-surface debris temperature through the summer monsoon on Khumbu Glacier, Nepal Himalaya

Morgan J. Gibson,[1]* Tristram D.L. Irvine-Fynn,[1] Patrick Wagnon,[2] Ann V. Rowan,[3] Duncan J. Quincey,[4] Rachel Homer[4] and Neil F. Glasser[1]

[1] Centre for Glaciology, Department of Geography and Earth Sciences, Aberystwyth University, SY23 3DB, UK
[2] University Grenoble Alpes, CNRS, IRD, Grenoble-INP, IGE, F-38000 Grenoble, France
[3] Department of Geography, University of Sheffield, S10 2TN, UK
[4] School of Geography, University of Leeds, LS2 9JT, UK

Received 9 September 2016; Revised 9 May 2018; Accepted 16 May 2018

*Correspondence to: Morgan J. Gibson; Centre for Glaciology, Department of Geography and Earth Sciences, Aberystwyth University, SY23 3DB, UK. E-mail: morganjgibson@gmail.com

ESPL
Earth Surface Processes and Landforms

ABSTRACT: Debris surface temperature is a function of debris characteristics and energy fluxes at the debris surface. However, spatial and temporal variability in debris surface temperature, and the debris properties that control it, are poorly constrained. Here, near-surface debris temperature (T_s) is reported for 16 sites across the lower elevations of Khumbu Glacier, Nepal Himalaya, for the 2014 monsoon season. The debris layer at all sites was ≥1 m thick. We confirm the occurrence of temporal and spatial variability in T_s over a 67-day period and investigate its controls. T_s was found to exhibit marked temporal fluctuations on diurnal, short-term (1–8 days) and seasonal timescales. Over the study period, two distinct diurnal patterns in T_s were identified that varied in timing, daily amplitude and maximum temperature; days in the latter half of the study period (after Day of Year 176) exhibited a lower diurnal amplitude (mean = 23°C) and reduced maximum temperatures. Days with lower amplitude and minimum T_s were concurrent with periods of increased seasonal variability in on-glacier air temperature and incoming shortwave radiation, with the increased frequency of these periods attributed to increasing cloud cover as the monsoon progressed. Spatial variability in T_s was manifested in variability of diurnal amplitude and maximum T_s of 7°C to 47°C between sites. Local slope, debris clast size and lithology were identified as the most important drivers of spatial variability in T_s, with inclusion of these three variables in the stepwise general linear models resulting in R^2 ≥0.89 for six out of the seven sites. The complexity of surface energy fluxes and their influence on T_s highlight that assuming a simplified relationship between air temperature and debris surface temperature in glacier melt models, and a direct relationship between debris surface temperature and debris thickness for calculating supraglacial debris thickness, should be undertaken with caution. © 2018 The Authors. Earth Surface Processes and Landforms published by John Wiley & Sons Ltd.

KEYWORDS: debris cover; surface temperature; ablation; Khumbu Glacier; Himalaya

Introduction

Debris-covered glaciers exhibit a continuous mantle of rock debris over the full width of at least some of their ablation zone (Kirkbride, 2011). These glaciers are common in mountainous regions across the world, including in the European Alps (Mihalcea *et al.,* 2006), Andes (Glasser *et al.,* 2016), Southern Alps of New Zealand (Kirkbride, 2000) and the Himalaya (Scherler *et al.,* 2011). The presence of a supraglacial debris layer influences glacier ablation, acting as a thermal buffer between the atmosphere and glacier ice surface, and modifying the energy available for melt (Jansson and Fredin, 2002; Kirkbride, 2000). The extent to which a supraglacial debris layer controls ablation is primarily dependent on the thickness of the debris layer (Clark *et al.,* 1994; Mattson, 2000; Østrem, 1959). While a thin layer of debris below a critical thickness causes an increase in ablation due to a reduction of the surface albedo (Nakawo and Rana 1999), ablation exponentially decreases with increasing debris thickness above a critical thickness, as the debris layer inhibits glacier melting by attenuating and reducing thermal energy transfer to the underlying ice surface (Brock *et al.,* 2010; Mihalcea *et al.,* 2008a; Nicholson and Benn, 2006; Reid *et al.,* 2012).

Supraglacial debris surface temperature is a function of the surface energy balance and modulates heat transfer through the debris layer (Nakawo and Young, 1981). Therefore, debris surface temperature can provide useful insight into the extent to which debris properties affect energy transfer at the surface of and through a debris layer. To date, little focus has been given to the influence of spatial and temporal variability in surface temperature across supraglacial debris layers, which can be affected by incoming energy fluxes and debris properties including albedo, surface roughness, sediment porosity, and

moisture content (Evatt *et al.,* 2015; Reznichenko *et al.,* 2010; Rounce *et al.,* 2015).

Nicholson and Benn (2013) highlighted the occurrence of spatial and temporal variability in supraglacial debris properties and their influence on surface temperature and temperature gradients through the debris layer, and therefore glacier mass balance. However, many of the previous studies concerned with the measurement of debris surface temperature on glaciers have had limited spatial or temporal extent. For example, Nakawo and Young (1982) measured debris surface temperature at six plots over a 48 h period, while Nicholson and Benn (2006) measured debris surface temperature at a maximum of 11 plots on one glacier, but only for a maximum period of 11 days. Steiner and Pellicciotti (2015) presented one of the most extensive debris surface temperature data sets to date, from 13 locations over three ablation seasons on Lirung Glacier, Nepal. However, the study focused on describing the relationship between air temperature (T_a) and debris surface temperature rather than exploring spatial variability in debris surface temperature. Moreover, Steiner and Pellicciotti (2015) did not state the thickness of the debris layer underlying each of the sensors measuring debris surface temperature, an important factor in the consideration of spatiotemporal variability in debris surface temperature and the influence of underlying ice (cf. Nicholson and Benn, 2006). Consequently, the nature of and controls on debris surface temperature variability remain poorly constrained in glacial environments.

Conversely, ground surface temperature variability has been relatively well studied in other cold region environments (Gubler *et al.,* 2011; Guglielmin, 2006; Romanovsky and Osterkamp, 2000) where significant spatial variation arises from localised changes in surface properties and environmental conditions. These studies have concluded that such variability influences the accuracy of surface energy balance modelling in these environments. We therefore contend that such variability may also be applicable to numerical modelling of debris-covered ice ablation and the response of these glaciers to climate change.

The importance of studies of debris surface temperature on debris-covered glaciers is manifested in the recent application of temperature-index models to debris-covered glaciers, which determine debris surface temperature from T_a (Carenzo *et al.*, 2016). Furthermore, debris surface temperature has previously been used to determine debris layer thickness through two approaches: the use of an empirical relationship between debris surface temperature and debris layer thickness, based on field data (Mihalcea *et al.,* 2008a, 2008b; Minora *et al.,* 2015); and a surface energy balance approach also using debris surface temperature (Foster *et al.,* 2012; Rounce and McKinney, 2014). Currently, neither approach has been considered robust, as the empirical approach is only applicable for debris layers thinner than 0.5 m (Mihalcea *et al.,* 2008a) and the energy balance approaches exclude consideration of spatially variable debris properties such as albedo, surface roughness or moisture content that will affect energy exchange and therefore surface temperature at the debris surface (Collier *et al.,* 2014; Evatt *et al.,* 2015; Rounce *et al.,* 2015). To understand the validity of these methods, and discern how to develop them further, confirmation of both the spatiotemporal regime of debris surface temperature and its controls is needed.

Considering these shortcomings, here we aimed to characterise the spatial and temporal variability in debris surface temperature on a debris-covered glacier using data collected from temperature sensors located in the debris near-surface and distributed over the lower ablation area of Khumbu Glacier, Nepal, in areas of thick (≥1 m) debris cover. The primary objectives of the study were to: (i) examine the temporal and spatial variation of debris surface temperature during an ablation season; and (ii) determine the controlling factors underlying variations in debris surface temperature.

Study area

Khumbu Glacier, Central Himalaya

Khumbu Glacier (27°56′N, 86°56′E) is ~17 km long and has an area of ~27 km^2 including the detached tributary glaciers, Changri Nup and Changri Shar (Figure 1: Bolch *et al.,* 2008; Arendt *et al.,* 2012; Vincent *et al.,* 2016). The glacier flows from the southwest flanks of Mount Everest at 8230 m above sea level (a.s.l.) descending to 4816 m a.s.l. The equilibrium line altitude (ELA) is situated at around 5700 m a.s.l. within the Khumbu Icefall (Benn and Lehmkuhl, 2000; Inoue, 1977). Khumbu Glacier is typical of many large Himalayan debris-covered glaciers, with a low-gradient (<2°), slow-flowing (<10 m a^{-1}) ablation area (Hambrey *et al.,* 2008; Quincey *et al.,* 2009). The glacier flows at ~70 m a^{-1} near the base of the icefall, while the lowermost 3–4 km is thought to flow at velocities below 10 m a^{-1} (Quincey *et al.,* 2009). Khumbu Glacier is in a state of negative mass balance; Bolch *et al.* (2011) calculated a surface change of –0.56 ± 0.13 m a^{-1} between 1956 and 2007, while King *et al.* (2017) calculated surface change across the glacier's ablation area of around –0.81 ± 0.16 m a^{-1} between 2000 and 2014.

The ablation area is almost entirely debris covered below 5400 m a.s.l., with the debris layer >2 m thick in places (Gades *et al.,* 2000). The debris-covered ablation area displays a wide range of clast sizes comprising of granitic and schistose lithologies derived from the surrounding hillslopes (Iwata *et al.,* 1980; Nuimura *et al.,* 2011). The debris-covered area is topographically complex and dynamic being characterised by an undulant surface punctuated by numerous supraglacial ponds and associated ice cliffs, which changes over seasonal and interannual timescales (Nuimura *et al.,* 2011; Watson *et al.,* 2016). The more stable, lowermost region of the ablation area shows the early stages of soil formation and is partially vegetated (Kadota *et al.,* 2000).

Central Himalayan climate

The South Asian Summer Monsoon (hereafter, 'the monsoon') dominates the climate of the Khumbu Glacier catchment, and the Central Himalaya. The highest annual air temperatures occur between May and October (Ageta, 1976; Nayava, 1974) and ~80% of precipitation falls between June and September (Bookhagen and Burbank, 2010). During the onset and progression of the monsoon season, high pressure over the Tibetan Plateau results in an increased temperature and pressure gradient southward towards the Indian subcontinent (Yasunari, 1976). This pressure gradient produces seasonally variable wind patterns in the Central Himalaya region and localised synoptic weather systems are dominated by mountain and valley winds, which vary on sub-diurnal timescales (Bollasina *et al.,* 2002). As the monsoon season progresses, increases in regional precipitation frequency, air temperature, relative humidity and incoming longwave radiation occur, and are coupled with a decrease in shortwave radiation attributed to increasing cloud cover (Salerno *et al.,* 2015; Shea *et al.,* 2015).

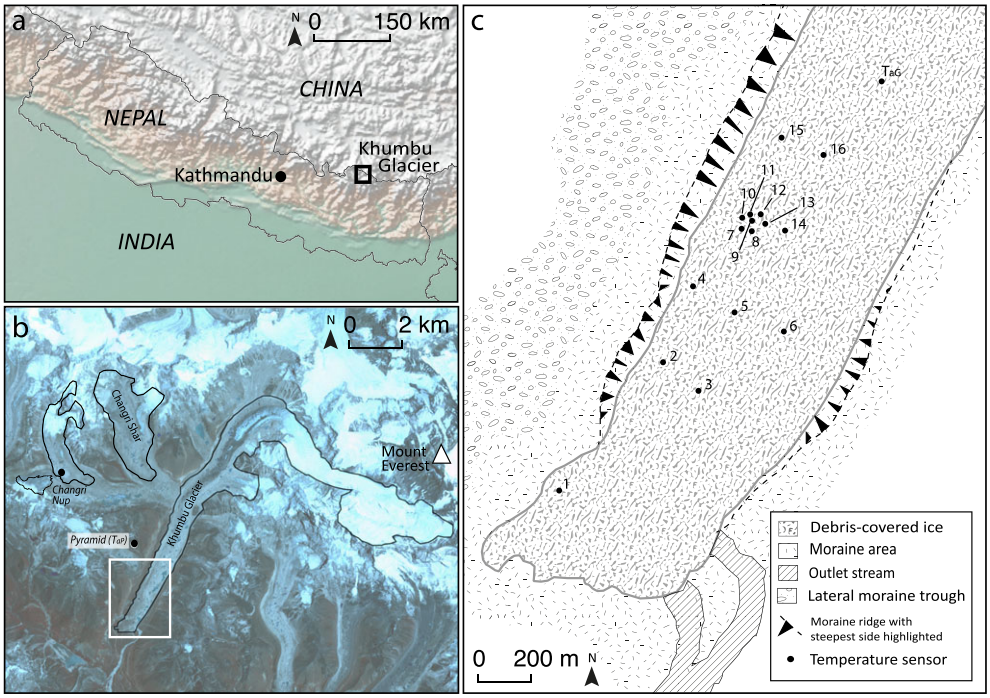

Figure 1. Study site location: (a) in a regional context; (b) in relation to Mt Everest, displaying the extent of Khumbu Glacier and location of the meteorological stations (Changri Nup and Pyramid) used in this study, including the extent of Changri Nup and Changri Shar (reproduced from Vincent *et al.,* 2016); (c) the study area and locations of temperature sensors, with corresponding temperature sensor ID, and on-glacier air temperature location (T_{aG}). [Colour figure can be viewed at wileyonlinelibrary.com]

Data acquisition

Near-surface debris temperature

Temperature sensors

Near-surface debris temperature (T_s) was measured as a robust proxy for true debris surface temperature using Maxim iButton™ Thermochron temperature sensors (model number DS1921G: http://datasheets.maximintegrated.com/en/ds/DS1921G.pdf), which record instantaneous temperature from –30 to +70°C with a manufacturer-stated accuracy of ±1.0°C. iButton sensors were chosen due to their low cost, reliability (Hubbart *et al.,* 2005) and previous successful applications in a number of environmental settings including permafrost landscapes (Gubler *et al.,* 2011). Gemini Tiny Tag™ Plus2 data loggers (model number TGP-4520) with encapsulated thermistor probes were used for sensor calibration prior to fieldwork and have a manufacturer–stated accuracy of ±0.4°C. The iButtons were placed in waterproof polycarbonate plastic containers to protect from water damage following the method of Gubler *et al.* (2011). The effect of polycarbonate plastic waterproof casing on temperatures recorded was tested in laboratory conditions prior to fieldwork. In laboratory conditions, temperatures recorded by contained and uncontained iButtons in the same environments varied by <2°C, and more typically by ≤0.5°C, which is within the manufacturer's stated accuracy (see Supplementary information; Figure S1).

Field experiment design

Near-surface debris temperature (T_s) was measured at hourly intervals at 16 sites between the 21 May and 29 July 2014 (Day of Year (DOY) 141 and 210). The first 48 h of each T_s timeseries were discarded to allow the sensors to equilibrate with local conditions. For all sites, iButtons were placed in the immediate near-surface of the debris layer, typically between 0.01 and 0.05 m below the surface, using a single layer of clasts of representative size for each site from the immediate surrounding area as a shield from direct solar radiation as is common practice in ground surface temperature studies (Apaloo *et al.,* 2012; Gisnås *et al.,* 2014). Using a handheld Garmin 64 GPS, the iButton temperature sensors were distributed across the lowermost 2 km^2 of Khumbu Glacier's ablation area in a gridded pattern (Figure 1(c)). The elevation of sensor sites varied across the study area by 49 m between 4903 m a.s.l. and 4952 m a.s.l. (±3 m due to vertical accuracy of the handheld GPS) and each site had a unique combination of site characteristics, varying in slope, aspect, elevation, clast size, sorting, roundness, and clast lithology (Table I; see also the section 'Ancillary data').

To allow examination of the influence of additional debris layer properties and incoming energy fluxes on T_s other than debris layer thickness, all iButton temperature sensors were installed in locations where the debris layer had a thickness of ≥1 m where the effect of cold propagation from underlying ice on T_s is insignificant (Foster *et al.,* 2012; Nicholson and Benn, 2006). Debris thickness was established by excavating the debris layer adjacent to the iButton location to a depth of 1 m; if no ice was present, debris thickness was reported as >1 m. At each site, a textural description of the debris was made, and digital photographs were taken before and after emplacement of the sensors (Figure 2). The iButton temperature sensors at Sites 7 to 13 were placed within a 90 × 90 m area to investigate variability in T_s across an area typical of the resolution of remotely sensed thermal satellite data (e.g. ASTER) often used for supraglacial debris thickness mapping.

On retrieval of the iButton temperature sensors at the end of the monsoon season, comparison with the initial site photographs was used to evaluate any surface change at each site. For all 16 sites reported, the debris showed little or no disruption after sensor installation, and none of the temperature sensors were exposed at the time of collection. A further 42 iButton sensors were installed on the glacier surface but, due to topographic change during the monsoon season, they could neither be located or retrieved.

Table I. Topographic and debris characteristics for iButton temperature sensor sites. Mean T_s uncertainty calculated for the near-surface placement of temperature sensors under representative clasts at each location. Rows highlighted in grey are timeseries identified to be less representative of T_s

Sensor ID	Elevation (m a.s.l.)	Debris description	Mean clast size (m)	Lithology (% granite)	Slope (°)	Aspect (°)	Curvature	Roughness ($\times 10^{-2}$; m)	Mean T_s uncertainty (°C)
1	4949	Large cobbles with medium sand matrix	0.058	100	10	202	-0.65	0.05	0.87
2	4952	Large cobbles with medium sand matrix	0.099	100	9	100	1.38	0.09	1.49
3	4945	Small to large cobbles with medium to coarse sand matrix	0.028	50	5	132	-0.82	0.19	0.42
4	4948	Small to large cobbles with coarse sand matrix	0.020	40	2	321	-1.46	0.09	0.3
5	4947	Large cobbles with medium to coarse sand matrix	0.029	50	5	285	-1.22	0.14	0.44
6	4952	Medium grained sand with < 5 % medium granite pebbles	0.002	100	3	173	-1.21	0.04	0.03
7	4949	Medium pebbles to large cobbles with medium sand matrix	0.020	50	5	224	-0.80	0.20	0.30
8	4903	Very coarse pebbles with medium sand matrix	0.010	95	12	290	0.17	0.04	0.15
9	4938	Small cobbles to large boulders with medium to coarse sand matrix	2.930	100	6	86	0.05	0.10	4.39
10	4938	Coarse pebbles to large boulders with consolidated medium sand matrix	0.027	50	6	266	0.88	0.04	0.41
11	4946	Small to large cobbles with consolidated medium to coarse sand matrix	0.055	70	5	103	0.57	0.11	0.83
12	4942	Small to large cobbles with medium to coarse sand matrix	0.016	60	6	125	0.49	0.03	0.24
13	4935	Small cobbles to large boulders with coarse sandy matrix	2.890	90	6	170	0.33	0.06	4.34
14	4937	Small cobbles to small boulders with coarse matrix	0.027	60	5	131	-1.15	0.30	0.41
15	4950	Very coarse pebbles to large cobbles with consolidated medium matrix	0.042	50	7	206	0.03	0.20	0.32
16	4949	Small cobbles to large boulders with medium to coarse sand matrix	0.030	50	8	274	0.11	0.15	0.30

Figure 2. Site photos before installation of temperature sensors: (a) Site 11: consolidated medium sand with medium pebbles; (b) Site 3: small cobbles to large boulders with a medium to coarse sand matrix; and (c) Site 15: small granite and schist cobbles to small boulders with course sand to medium pebble matrix. [Colour figure can be viewed at wileyonlinelibrary.com]

Despite following standard methods for measuring ground surface temperature (Apaloo *et al.,* 2012; Gisnås *et al.,* 2014), placing clasts on the contained iButtons to shield them from direct incoming shortwave radiation created an additional source of uncertainty in the 16 retrieved T_s data. Consequently, our measurements of T_s do not necessarily reflect absolute debris surface temperature (Conway and Rasmussen, 2000) as the emplacement of sensors beneath clasts may mean that the sensors record temperature below rather than at the debris surface. Without detailed knowledge of the specific thermal properties of the debris at each site, more accurate assessment of the uncertainty between near-surface and true surface temperature is challenging. However, here we assumed our T_s data were sound proxies for absolute T_s. To identify any data which were likely to be less representative of true surface temperature, uncertainty at each site was estimated using the diurnally-averaged temperature gradient calculated through a debris layer by Nicholson and Benn (2006) from data collected on nearby Ngozumpa Glacier of –10.5°C m^{-1}, and mean clast size for each site. These uncertainties ranged from 0.03°C to 4.39°C (Table I). Temperature metrics (mean T_s, maximum T_s, minimum T_s and T_s amplitude) were also regressed against estimated sensor depth. No significant relationship was identified meaning T_s variability between sites cannot be attributed directly to sensor depth. Consequently, sites at which the calculated near-surface to surface temperature difference was greater than 0.5°C (the assessed uncertainty in our iButton sensor data) were considered to be less reliable in reflecting absolute surface temperature (Sites 1, 2, 9, 11 and 13), and were therefore either noted or omitted from subsequent analyses to avoid potential influence of misrepresentative data.

Mean clast size was considered a proxy for sensor burial depth, although it is probable that clasts covering the sensors were smaller than the mean clast size as a bias towards the smaller clasts would have occurred on emplacement. It is therefore expected the uncertainty calculated using mean clast

size overestimates burial depth, and consequently the uncertainty in temperature with depth is less than estimated. However, this method of uncertainty calculation does not include consideration of diurnal variability in temperature gradient through the debris layers, which may cause mean temperature differences calculated here to be larger at certain times of day (as observed by Nicholson and Benn, 2006). The influence of this diurnal variability on results is discussed in the section 'Spatial variability in near-surface debris temperature'.

Ancillary data

Clast size and lithology

Clast size at each site was estimated from 18.0 Mpix digital site photographs acquired using a Canon 550D camera and processed in ImageJ, v. 1.49 (Rasband, 2008), following the method outlined by Igathinathane *et al.* (2009). At all sites, images covered approximately 1 m^2 and a known scale in each photograph was used to define the metre: pixel ratio. Clasts were selected using a random sampling method. For each site photo, every clast identified was assigned a number, and a random number generator was used to subsample 25 clasts for measurement within ImageJ. Assuming from the 2D imagery that the long and intermediate clast axes were visible, the intermediate axis length was retrieved and a mean representative clast size for each site calculated (Table I). Where the intermediate axis of a clast was larger than the photo (Sites 9 and 13) the maximum length measurable from the scaled image was used.

Clast lithology was determined in the field using clast size, colour and mineral composition. Two major lithologies were identified; granite and schist. The dominant lithology at each site (Table I) was determined by manually classifying the lithology of all clasts in each of the site photographs in ImageJ and then calculating the percentage of granite for each site (Solano *et al.,* 2016).

Local meteorological data

Meteorological data were collected at four locations: on the debris-covered glacier surface of Khumbu Glacier at an elevation of 4950 m a.s.l. (Figure 1(c)); at the Pyramid Observatory (Figure 1(b); 27°57′32″ N, 86°48′47″ E; 5050 m a.s.l.) ~1 km to the northwest of the study area; an automatic weather station on a debris-covered area of the adjacent Changri Nup Glacier (Figure 1b; 27°58′55″N, 86°45′52.92″ E; 5363 m a.s.l.); and at an automatic weather station 5 km down-valley from the terminus of Khumbu Glacier at Pheriche (27°53′24″ N, 86°49′12″ E; 4260 m a.s.l.).

Off-glacier air temperature (T_{aP}) was recorded at hourly intervals 2 m above the ground surface, using an artificially ventilated LSI-Lastem DMA 570 sensor (accuracy ±0.2°C) at the Pyramid Observatory. On-glacier air temperature (T_{aG}) was recorded at 30 min intervals in a location with schistose debris lithology (Figure 1(c)) using a Gemini Tiny Tag™ Plus2 data logger (model number TGP–4520) and thermistor probe with a stated accuracy of ±0.2°C. The on-glacier thermistor probe was placed in a naturally aspirated radiation shield mounted on a tripod 1 m above the debris surface. T_{aG} was resampled to give hourly values corresponding to the resolution of the T_s data. Incoming shortwave (SW_{in}) and longwave (LW_{in}) radiation (Kipp&Zonen CNR4 sensor, 1.0 m above debris surface, stated accuracy ±3%) and relative humidity data (RH: Vaisala HMP45C sensor, 2.15 m above debris surface, stated accuracy ±2%) were recorded at an automatic weather station at the Changri Nup Glacier. Meteorological data from the Changri Nup station were collected at 30 min intervals and resampled to 1 h resolution using an hourly mean algorithm. Precipitation (P) was measured using a Geonor T-200 all-weather rain gauge at the Pheriche site where summer precipitation predominantly occurs as rainfall; these data were corrected for undercatch of solid precipitation using air temperature and wind speed (Sherpa *et al.,* 2017) and the resultant corrected data have an estimated accuracy of ±15%.

Local topography

The digital elevation model (DEM) from which slope and aspect were extracted for each sensor site was derived from a series of Surface Extraction from Triangulated Irregular Network Searchspace Minimization (SETSM) DEMs sourced from the Polar Geospatial Centre (University of Minnesota) at 8 m resolution, collected between 8 February and 4 May 2015 (Noh and Howat, 2015). The DEM correction method is detailed in King *et al.* (2017). Due to the complex and dynamic nature of the glacier surface, topographic parameters at each iButton site were estimated *a posteriori* from the DEM and are presented here as a generalised local proxies rather than absolute, site-specific values (Table I). Slope (in degrees) and terrain curvature were extracted for the pixels corresponding to the sensor locations using ESRI's ArcMap v10.1 Spatial Analyst toolbox. Relative terrain roughness was derived using the 'vector ruggedness measurement toolbox', which considers slope and aspect variability for the nine pixels on and around each site location (Sappington *et al.,* 2007). Curvature and roughness metrics both ranged between –1 and +1. *In situ* observations of the local aspect of each iButton site, measured relative to north, were collected in the field using a magnetic compass with an uncertainty of ± 2°.

Results

Near-surface debris temperature

Daily mean near-surface debris temperature (T_s) for all 16 sites typically exceeded air temperatures (T_{aP} and T_{aG}) throughout the monsoon period (Figure 3(a)). Mean T_s for the period of observations at the 16 sites ranged from 7.0 to 11.6°C. T_s remained close to 0°C between DOY 146 and 152, which was coincident with heavy snowfall in Khumbu valley and the ensuing persistence of a ~0.4 m snow layer on the glacier surface. Following DOY 152, the snow cover melted, with the rate and timing of the return to T_s >5°C at each site highly varied. Subsequently, from DOY 156 onwards, all T_s timeseries exhibited a broadly similar quasi-parallel pattern of change until the end of the observation period. T_s appeared to follow a generally rising trend from DOY 156–166, and then a seasonal decrease of approximately –0.1°C d^{-1} until DOY 210. However, these seasonal rising and falling trends were superimposed with 5 to 8 day cycles in T_s, potentially reflecting synoptic variations, and intermittent, shorter (1–3 day) periods with lowered T_s. At all 16 sites, T_s exhibited marked diurnal variation (Figure 3(b)). Zero amplitudes persisted during the brief period of snow cover (DOY 147–151), the highest daily amplitudes of up to 47°C were found before DOY 170, and progressively declining amplitudes (reducing to a mean of 15°C) characterised the period following DOY 170. Over the monsoon season, the contrasts in T_s between the sites were greatest at the start of our observations and between DOY 153 and 170, and declined thereafter, with the least difference between sites seen during the short periods of reduced T_s.

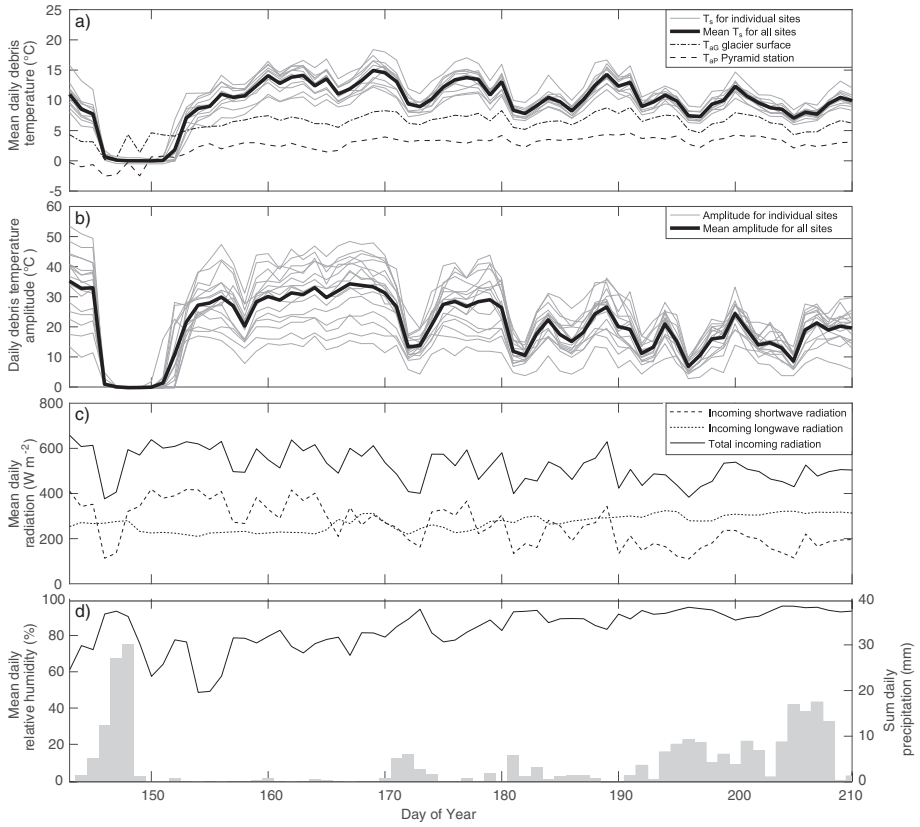

Figure 3. (a) Mean diurnal T_s for all temperature sensor sites, alongside on- and off-glacier air temperature timeseries, (b) daily amplitude in T_s at all sites; (c) mean daily incoming shortwave, longwave and total radiation (SW_{in}, LW_{in} and NR_{in}, respectively); (d) total daily precipitation and mean daily relative humidity across the study period.

Meteorology

Mean daily on- and off-glacier air temperature (T_{aG} and T_{aP}) followed a similar, but subdued, pattern to the T_s data (Figure 3(a)). Air temperature increases of the order of 3°C occurred over the entire study period in both T_{aP} and T_{aG}. The seasonal pattern in T_{aG} and T_{aP} was overlain by a subtle synoptic periodicity with a 5–8 day recurrence. The diurnal amplitudes seen in the T_a series were less than those observed for T_s. Daily variation in amplitude ranged from 2.1 to 10.4°C for T_{aP}, and from 5.4 to 20.2°C for T_{aG}. In both T_a records, diurnal amplitude was greatest during the period of snow cover, and showed a general reduction over the course of the observation period albeit punctuated by short (1–3 day) variability. Off-glacier T_{aP} was consistently lower than on-glacier T_{aG} by a mean difference of 5°C between DOY 145 and 190, and 3°C from DOY 190 onwards.

Mean daily SW_{in} displayed an overall seasonal decrease from 405 W m^2 to ~217 W m^2 over the observation period, with short-term (<5 days) variability of the order of 200 W m^2 over the study period (Figure 3(c)). Between DOY 148 and 149, SW_{in} was lowest at 123 W m^2, which corresponded to snowfall and a coincident decrease in T_s to 0°C. In contrast, mean daily LW_{in} increased from 253 W m^2 to 320 W m^2 from DOY 143 to 210. Total net incoming radiation (NR_{in}) was primarily influenced by the pattern of SW_{in}. All three series of radiative energy displayed synoptic (3–8 days) and short-term (1–3 day) variability. Relative humidity displayed a seasonally increasing trend from around 60% on DOY 143 to around 95% by the end of the observation period; this seasonal change was superimposed with shorter-term variability including a brief increase in relative humidity (to >80%) between DOY 146 and 150, aligned with the snowfall and snow cover event (Figure 3(c)). During the snowfall event, total daily precipitation peaked on DOY 150 at 34 mm, but subsequently remained low until DOY 170 and then, as the monsoon progressed further, the magnitude and frequency of precipitation events increased (Figure 3(d)). Increases in total daily precipitation were typically concurrent with decreased SW_{in} and increased LW_{in} and relative humidity.

Timeseries Analyses

A Kolmgorov-Smirnov normality test showed that none of the temperature timeseries (T_s or T_a) were normally distributed at 95% confidence level. Therefore, non-parametric analyses were required to interrogate these data further.

Comparison of timeseries

The overall average of mean and standard deviation of T_s for all timeseries was 9.2 ±1.3°C, or 9.6 ±1.2°C if the data considered less representative of T_s were excluded. Analytical tests indicated that the mean T_s timeseries was highly correlated with both T_{aP} (Spearman's $r = 0.85$, $P < 0.05$) and T_{aG} ($r = 0.78$, $P < 0.05$) but was significantly higher than both the two T_a timeseries.

The broad similarity in the individual T_s timeseries (Figure 3(a), (b); Figure 4) was highlighted by strong and significant correlation coefficients for the majority of site pairs (Table II). The generally high correlation ($r \geq 0.88$) between timeseries indicated that all sites exhibited a broadly similar general pattern in both periodicity and seasonal trend. However, further comparison using a Kruskal–Wallis test (which tests whether samples originate from the same distribution) showed the T_s populations were significantly different ($\chi^2 = 308.9$, or $\chi^2 = 201.1$ excluding the timeseries that were less

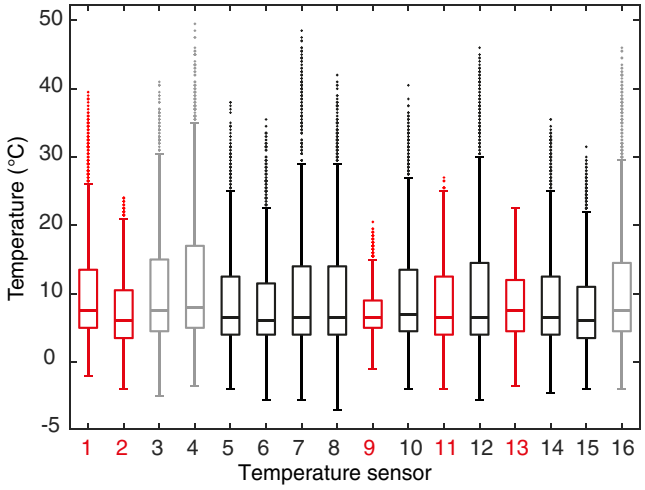

Figure 4. Box plots of mean, interquartile range, maximum and minimum near-surface debris temperature for each of the timeseries. Red box plots are the timeseries identified as timeseries less representative of T_s, greyed plots are timeseries identified as significantly different from the statistically representative Site 14. Outliers are considered to be values outside of the range between the 25th and 75th percentiles. [Colour figure can be viewed at wileyonlinelibrary.com]

representative of T_s, both $P << 0.05$). To explore the underlying nature and causes for these differences, we: (i) examined the temporal variability in the T_s series; (ii) conducted a more detailed assessment of the spatial differences between timeseries; and (iii) explored any associations between T_s and the local meteorological and site-specific data. Each of these three sets of analyses are detailed in the following sections.

Temporal variability in near-surface debris temperature

The similarity in the daily T_s means and their seasonal pattern, with the exception of the period of snowfall (DOY 146–152), was underlain by a marked reduction in the daily amplitude of variability in T_s at all sites over the study period (Figure 3(b)). To test this observation further, regression analysis was employed, with omission of data from the snowfall period. Sites 1, 4, 7, 10, 12 and 16 showed a significant ($P < 0.05$) decrease in daily mean T_s over the observation period, while all other sites showed no such temporal trend (Table III). However, all sites showed a statistically significant increase in daily minimum T_s during the monsoon season, averaging 0.08°C d^{-1}; and with the exception of Site 13, all sites also showed a significant decrease in daily maximum temperature (mean –0.19°C d^{-1}). The concomitant increase in minimum and decreasing maximum T_s between timeseries was reinforced by the significant decreasing trend in daily amplitude by a mean of –0.26°C d^{-1} over the monsoon period at all 16 sites (Table III). These changes were in contrast to air temperature trends, where daily minimum and mean T_{aG} increased by 0.1°C d^{-1} and 0.04°C d^{-1}. No significant trend in mean daily maximum T_{aG}, was present, although daily amplitudes decreased by –0.1°C d^{-1}.

To further examine these seasonal trends in T_s amplitude, and to ascertain if there was systematic change in the diurnal pattern of T_s fluctuation, we adopted the approach commonly used to analyse synoptic climatology (Brazel *et al.,* 1992; Davis and Kalkstein, 1990), hydrological timeseries (Hannah *et al.,* 2000; Irvine-Fynn *et al.,* 2005; Swift *et al.,* 2005) and ground surface temperature (Lundquist and Cayan, 2007). These previous published analyses used principal components analysis (PCA) to classify patterns of change or modes of variation in diurnally fluctuating timeseries. Here, rather than analyse all 16 T_s timeseries, and given the high correlation between all sites (excluding timeseries less representative of T_s) (Table II), a 'representative' timeseries from the data set was used. The most representative T_s timeseries was identified using a Nash-Sutcliffe efficiency coefficient (*E*) typically used to determine the fit of modelled to observed data (Krause *et al.,* 2005; Legates and McCabe, 1999). *E* was calculated for each T_s pair and then summed and averaged for each individual site (Table II). The timeseries with the highest similarity to all other T_s series was from Site 14 ($\sum E$ = 12.4, mean *E* = 0.83), and was therefore considered representative.

Table II. A matrix of Spearman rank correlation coefficient (*r*) and Nash–Sutcliffe efficiency coefficient (*E*) for each pair of raw (hourly) T_s timeseries. All correlations displayed $P < 0.05$. The greyed rows (Sites 1, 2, 9, 11 and 13) are those identified as being less representative of debris surface temperature due to site clast size. Correlation between each raw T_s series and the mean T_s is shown, along with the sum and average *E* for each

		Spearman's correlation coefficient (*r*)																
	Sensor ID	1	2	3	4	5	6	7	8	9	10	11	12	13	14	15	16	Mean T_s
Efficiency criterion (E)	**1**		0.96	0.96	0.98	0.97	0.97	0.97	0.92	0.94	0.96	0.95	0.97	0.96	0.97	0.94	0.98	0.98
	2	0.30		0.96	0.95	0.97	0.94	0.95	0.88	0.97	0.95	0.97	0.96	0.96	0.98	0.98	0.97	0.97
	3	0.93	0.69		0.97	0.94	0.97	0.98	0.95	0.92	0.98	0.99	0.98	0.92	0.99	0.96	0.97	0.99
	4	0.91	0.52	0.92		0.95	0.97	0.97	0.95	0.91	0.97	0.96	0.98	0.94	0.97	0.93	0.97	0.99
	5	0.93	0.80	0.84	0.63		0.95	0.96	0.88	0.95	0.94	0.93	0.96	0.94	0.96	0.96	0.98	0.96
	6	0.80	0.81	0.75	0.39	0.87		0.99	0.95	0.9	0.98	0.96	0.99	0.9	0.97	0.94	0.97	0.99
	7	0.91	0.63	0.94	0.91	0.86	0.82		0.95	0.91	0.98	0.96	0.99	0.92	0.98	0.95	0.98	0.99
	8	0.82	0.57	0.84	0.75	0.77	0.80	0.79		0.84	0.96	0.93	0.95	0.86	0.93	0.89	0.91	0.96
	9	-0.12	0.65	-0.17	-0.36	-0.42	-0.04	-0.28	-0.19		0.92	0.93	0.92	0.95	0.94	0.94	0.93	0.93
	10	0.92	0.72	0.94	0.81	0.90	0.89	0.87	0.87	0.53		0.97	0.99	0.92	0.98	0.95	0.97	0.99
	11	0.66	0.90	0.68	0.16	0.77	0.84	0.35	0.45	0.70	0.75		0.97	0.93	0.98	0.97	0.96	0.98
	12	0.90	0.66	0.94	0.91	0.86	0.80	0.96	0.81	0.44	0.93	0.77		0.93	0.99	0.96	0.98	1.00
	13	0.37	0.86	0.20	-0.48	0.58	0.60	-0.33	-0.11	0.75	0.35	0.81	-0.20		0.94	0.92	0.94	0.94
	14	0.87	0.84	0.90	0.66	0.91	0.88	0.80	0.66	0.60	0.90	0.91	0.85	0.80		0.98	0.98	0.99
	15	0.65	0.92	0.65	0.13	0.83	0.84	0.40	0.32	0.71	0.70	0.92	0.47	0.80	0.89		0.97	0.96
	16	0.90	0.65	0.94	0.89	0.86	0.78	0.92	0.70	0.41	0.88	0.75	0.94	0.64	0.91	0.78		0.99
	$\sum E$	10.75	10.52	10.99	7.75	10.99	10.83	9.55	8.85	3.21	11.96	10.42	11.04	5.64	12.38	10.01	11.95	
	Mean *E*	0.72	0.7	0.73	0.52	0.73	0.72	0.64	0.59	0.21	0.8	0.69	0.74	0.38	0.83	0.67	0.8	

Table III. Results of regression analyses to identify seasonal trends in minimum, mean, maximum T_s and the associated daily amplitude. Seasonal trend slope (b, in °C d^{-1}) is given with the associated *P*-value, and statistically significant slopes are indicated in *italic*. The greyed rows are those identified as timeseries less representative of T_s

	Daily minimum T_s		Daily mean T_s		Daily maximum T_s		Daily amplitude T_s	
Sensor ID	b	*p*	b	*p*	b	*p*	b	*p*
1	0.06	<< 0.05	-0.03	< 0.03	-0.22	<< 0.05	-0.28	<< 0.05
2	0.07	<< 0.05	-0.01	0.53	-0.11	<< 0.05	-0.18	<< 0.05
3	0.08	<< 0.05	-0.03	0.06	-0.22	<< 0.05	-0.30	<< 0.05
4	0.08	<< 0.05	-0.05	< 0.05	-0.28	<< 0.05	-0.36	<< 0.05
5	0.07	<< 0.05	-0.02	0.07	-0.20	<< 0.05	-0.27	<< 0.05
6	0.08	<< 0.05	-0.01	0.60	-0.19	<< 0.05	-0.27	<< 0.05
7	0.10	<< 0.05	-0.06	<< 0.05	-0.37	<< 0.05	-0.47	<< 0.05
8	0.10	<< 0.05	-0.01	0.55	-0.17	<< 0.05	-0.27	<< 0.05
9	0.03	<< 0.05	0.00	0.62	-0.09	<< 0.05	-0.12	<< 0.05
10	0.06	<< 0.05	-0.04	< 0.05	-0.18	<< 0.05	-0.24	<< 0.05
11	0.08	<< 0.05	0.00	0.80	-0.10	< 0.05	-0.18	<< 0.05
12	0.10	<< 0.05	-0.04	< 0.05	-0.26	<< 0.05	-0.36	<< 0.05
13	0.05	<< 0.05	-0.01	0.61	-0.03	0.11	-0.09	<< 0.05
14	0.08	<< 0.05	-0.03	0.06	-0.18	<< 0.05	-0.27	<< 0.05
15	0.08	<< 0.05	0.00	0.92	-0.11	< 0.05	-0.19	<< 0.05
16	0.08	<< 0.05	-0.05	< 0.05	-0.28	<< 0.05	-0.36	<< 0.05
Mean	**0.08**	-	**-0.02**	-	**-0.19**	-	**-0.26**	-

Debris temperature data from Site 14 were divided into individual diurnal periods of 24 measurements commencing at midnight (00:00). Diurnal periods in which T_s was consistently 0°C (DOY 146 to 152) due to lying snow cover were omitted from the analysis. The resultant 61 diurnal data series were reduced and simplified into a number of 'modes' of variation, or principal components (PCs), using PCA without rotation. The first two PCs provided the primary modes of diurnal variation in T_s (Figure 5(a)). PC1 accounted for 81.3% of the variance and PC2 for 8.8%. The remaining PCs were discounted as 'noise' because they represented less than 10% of the total variance in the data set (Hannah *et al.,* 2000; Irvine-Fynn *et al.,* 2005). Although absolute loadings were relatively weak (<0.5) for both PCs, a total of 30 days were described best by PC1 and 19 days associated with PC2. A total of 11 days were very weakly related to either PC1 or PC2 (absolute loadings of < 0.09), and were considered to have an undefined diurnal T_s cycle (Figure 5(b), (c)). Of note were the 11 days described by negative loadings on PC2, which contrasted with the consistently positive loadings for PC1, and were suggestive of lagged relationships between the mode of variation and true diurnal T_s pattern. Days associated with PC1 predominantly occurred during the former half of the observation period (76% before DOY 176), while 78% of days associated with PC2 and 90% of days with an undefined cycle both occurred following DOY 176 (Figure 5(c)).

The contrast between the days assigned to the two main PCs and the undefined diurnal cycles were illustrated through a comparison of descriptive statistics (Table IV). The mean diurnal T_s was greatest for those days defined by PC1 at 10.9°C, while the mean maximum temperature and diurnal amplitude

Table IV. Descriptive statistics for groups of days corresponding to each of the key principal components (PCs) and undefined diurnal cycles, identified through PCA. Standard deviations are given in brackets

Descriptor	PC 1	PC 2	Undefined
Number of days represented by PC	30	19	11
Mean daily T_s (°C)	10.9 (1.9)	9.5 (1.8)	7.9 (1.5)
Mean maximum T_s (°C)	29.8 (3.6)	23.3 (6.0)	16.8 (4.4)
Mean minimum T_s (°C)	0.9 (2.5)	3.3 (1.4)	3.4 (1.4)
Mean T_s amplitude (°C)	28.9 (4.1)	20.1 (6.7)	13.5 (4.1)
Mean time of peak T_s (h)	13:06 (±1:12)	13:24 (±1:06)	13:12 (±1:42)

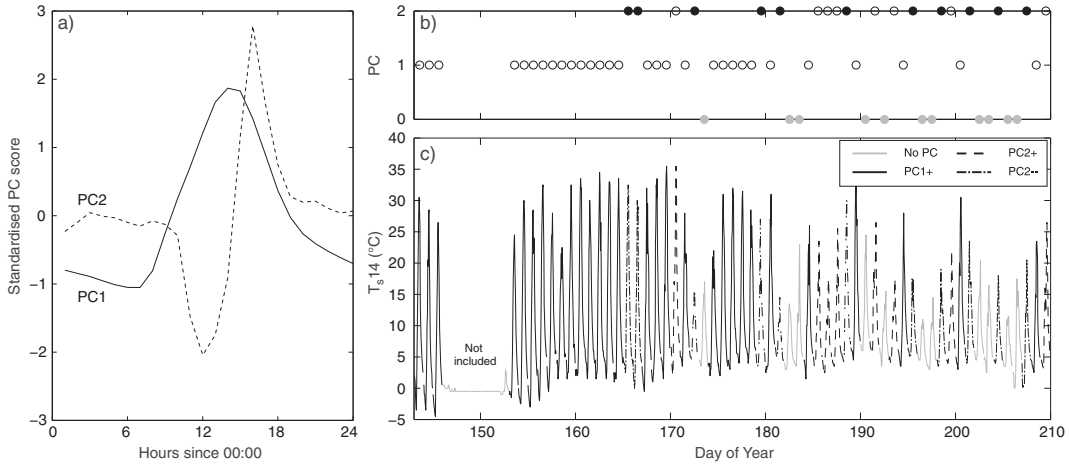

Figure 5. (a) The two modes of variability in T_s for Site 14, described by PC1 and PC2; (b) plot to identify days described by PCs 1 or 2, filled circles identify days with a negative or lagged relationship to PC2 and greyed circles mark days not described by either dominant PC; (c) T_s timeseries for Site 14 highlighting each day's mode of variation.

was highest compared with days with an undefined T_s variation and those associated with PC2. Days that were best described by PC2 exhibited relatively low mean daily amplitude, and mean and maximum diurnal temperatures. The 11 days that were less well defined by PCs had lowest mean, maximum and amplitude in T_s. Days described by PC1 were characterised by a lower mean minimum T_s (0.9°C) while all other days experienced similar minimum values of T_s. The mean time at which T_s peaked for each group of days associated with the PCs varied by less than one hour (Table IV).

Subtle variation in diurnal patterns was present in the T_s timeseries. There was a clear progressive shift during the monsoon season towards T_s exhibiting a lower daily mean, maximum and amplitude, but with a seasonal increase in the minimum T_s. The combination of *E* and PCA analyses explored this further, showing that all sites displayed a regular diurnal pattern of T_s during the former part of the monsoon, while there was a systematic shift to more variable and delayed diurnal cycles in the latter half of the observation period. These shifts in magnitude of T_s were aligned with the observed seasonal changes in meteorological conditions, specifically with increased precipitation, relative humidity and LW_{in} from around DOY 180.

Spatial variability in debris surface temperature

With evidence of spatial variability between sites most clearly evidenced by the differences in diurnal amplitude between the T_s timeseries, further exploration of the spatial contrasts was undertaken. Following the identification of significant difference by a Kruskal–Wallace test, a signed rank pairwise Wilcoxon test provided further detail on spatial variations by comparing pairs of timeseries populations. The representative series from Site 14 was the most similar to all other timeseries, being statistically dissimilar to only Sites 1, 3, 4 and 16 (Table II). Removal of the timeseries considered as less representative of T_s made relatively minimal difference to the analysis, suggesting that even the outlying data (Sites 2, 9, 11, 13) were broadly similar to the remaining T_s despite the uncertainty arising from varying depth of sensors. A further set of Wilcoxon tests were undertaken on the positively skewed distribution series of maximum, minimum and mean diurnal amplitude of T_s. The results of the site comparison data showed 86% and 89% of site pairs had significantly different diurnal amplitudes and maximum T_s from one another ($P < 0.05$), while 39% of the site pairs displayed significantly different minimum T_s ($P < 0.05$).

Daily mean minimum T_s for all timeseries varied by –1°C to –4°C between sites, while daily mean maximum T_s varied between 10°C and 17°C. While non-parametric correlation coefficients (*r*) suggested minimal variability between sites with 86% of correlations displaying $r \geq 0.90$ (Table II), such correlations only reveal similarity in timeseries patterns rather than magnitude (Borradaile, 2013). Consequently, notwithstanding the sensitivity of the efficiency criterion (Krause *et al.,* 2005), *E* was used to compare the strength of each relationship with regards to similarity in both value and pattern for the T_s timeseries (Table II). The *E* values displayed high variability and ranged from –0.42 (Sites 5 and 9) to 0.96 (Sites 7 and 12). The timeseries less representative of T_s displayed predominantly lower *E* values, particularly in their relationships with each other. Spatial variability between the sites appeared relatively small with 84% of *E* values ≥0.75, suggesting a good similarity in pattern and magnitude between pairs of T_s timeseries. For sites located in close proximity to one another (Sites 7–13, omitting those that were less representative of T_s) all the site pairs displayed $r \geq 0.87$ and 80% of these site pairs displayed an *E* value ≥0.81. However, the contrast in *E* between timeseries suggests subtle spatial variability in T_s did exist between study sites. The correlations between T_s remained high (>0.87) even when they were detrended to remove diurnal cycles (following Kristoufek, 2014). This further shows that T_s exhibited similar short-term and seasonal variations despite varying sensor locations.

Cross-correlation between the detrended timeseries was used to identify any lag between T_s (Table V). Lag times were present for Sites 1 and 2 and a number of other different sites, and with both Sites 8 and 15 for a number of sites. All sites lagged the timeseries at Site 8 by 1 or 2 h, while Site 15 displayed a 1 h lag with 7 sites. Site 8 and 15 were located under 0.010 m and 0.042 m of debris, neither of which are sites where mean clast size, and therefore burial depth, were greatest, and neither sites had been identified as less representative of T_s or statistically dissimilar. With regards to the site characteristics, Site 8 was placed in the most northerly aspect and lowest elevation of all iButton locations, while Site 15 had one of the highest elevations and roughness metrics (Table II). Despite a broad statistical similarity in the T_s data, there were a number of contrasts in the magnitude, distribution

Table V. Correlation coefficient and lag time for pairs of detrended T_s timeseries for which the persistent 24-h diurnal cycles have been removed. The grey rows are those identified as being less representative of debris surface temperature due to site clast size

	Correlation coefficient (*r*)															
	Ts1	Ts2	Ts3	Ts4	Ts5	Ts6	Ts7	Ts8	Ts9	Ts10	Ts11	Ts12	Ts13	Ts14	Ts15	Ts16
Ts1		0.95	0.98	0.99	0.99	0.98	0.98	0.94	0.95	0.98	0.96	0.98	0.93	-0.97	0.95	0.97
Ts2	-1		0.96	0.94	0.96	0.93	0.93	0.84	0.98	0.94	0.98	0.96	0.97	0.98	0.99	0.97
Ts3	0	0		0.99	0.98	0.99	0.98	0.94	0.94	0.99	0.98	0.99	0.92	0.98	0.97	0.98
Ts4	0	1	0		0.98	0.99	0.98	0.95	0.94	0.99	0.96	0.98	0.92	0.97	0.94	0.97
Ts5	0	0	0	0		0.98	0.98	0.92	0.97	0.98	0.97	0.98	0.94	0.98	0.97	0.98
Ts6	0	1	0	0	0		0.99	0.96	0.92	0.99	0.95	0.98	0.89	0.96	0.94	0.97
Ts7	0	1	0	0	0	0		0.95	0.92	0.99	0.96	0.99	0.87	0.97	0.95	0.98
Ts8	1	2	1	1	1	1	1		0.85	0.96	0.90	0.94	0.82	0.89	0.86	0.90
Ts9	0	0	0	-1	0	0	0	-1		0.93	0.96	0.94	0.97	0.96	0.96	0.95
Ts10	0	1	0	0	0	0	0	-1	0		0.97	0.99	0.91	0.97	0.95	0.97
Ts11	0	0	0	0	0	0	0	-1	0	0		0.98	0.95	0.99	0.98	0.97
Ts12	0	0	0	0	0	0	0	-1	0	0	0		0.92	0.99	0.97	0.99
Ts13	0	0	0	0	0	0	0	-1	0	0	0	0		0.94	0.94	0.93
Ts14	0	0	0	0	0	0	0	-1	0	0	0	0	0		0.99	0.99
Ts15	-1	0	-1	-1	-1	-1	-1	-2	0	-1	0	0	0	0		0.98
Ts16	0	0	0	0	0	0	0	-1	0	0	0	0	0	0	0	
	Lag time (hours)															

Table VI. Results of SMR models describing natural logarithm transformed T_s timeseries (*T_s) from meteorological variables and additional predictors derived from the meteorological timeseries (see text for full details). Predictive variable importance (e.g. 1, 2, etc.) or sequence (e.g. variables 1+2, or all indicated by +3+) is shown, with coefficients of determination and root mean squared error for each model given in parentheses (R^2, RMSE). The grey rows are those identified as being less representative of debris surface temperature due to site clast size

	SMR 1: raw transformed meteorological variables				SMR 2: minus *T_{aG}			SMR 3: combined radiation minus *T_{aG}				SMR 4: Alternatives to T_{aG}
Site	*T_{aG}	*SW_{in}	*LW_{in}	*RH	*SWin	*SWin +*LWin, *RH, *P	*NR	*NR+dT_a	+All *RH, ∑SWin, ∑LWin, *P, tP	All *RH, *P, tP
1	1 (0.59, 0.373)	2 (0.60, 0.368)	3 (0.60, 0.367)	4 (0.62, 0.358)	1 (0.33,0.476)	1+ (0.45, 0.432)	1 (0.37, 0.462)	1+2 (0.45, 0.432)	+3+ (0.49, 0.415)	+3+ (0.69, 0.325)
2	1 (0.47, 0.313)	2 (0.50, 0.304)	3 (0.52, 0.298)	4 (0.55,0.287	1 (0.21, 0.383)	1+ (0.39, 0.335)	1 (0.26, 0.370)	1+2 (0.38, 0.339)	3+ (0.42, 0.328)	+3+ (0.62, 0.265)
3	1 (0.55, 0.342)	2 (0.57, 0.335)	3 (0.57, 0.333)	4 (0.59, 0.325	1 (0.27, 0.433)	1+ (0.40, 0.394)	1 (0.32, 0.422)	1+2 (0.37, 0.405)	+3+ (0.42, 0.387)	+3+ (0.63, 0.311)
4	1 (0.61, 0.362)	2 (0.62, 0.360)	4 (0.64, 0.349)	3 (0.62, 0.357)	1 (0.35, 0.466)	1+ (0.46, 0.425)	1 (0.39, 0.453)	1+2 (0.43, 0.438)	+3+ (0.48, 0.418)	+3+ (0.67, 0.334)
5	1 (0.53, 0.344)	4 (0.57, 0.329)	2 (0.55, 0.338)	3 (0.56, 0.334)	1 (0.28, 0.426)	1+ (0.41, 0.385)	1 (0.32, 0.412)	1+2 (0.42, 0.381)	+3+ (0.45, 0.371)	+3+ (0.65, 0.297)
6	1 (0.56, 0.289)	4 (0.60, 0.277)	2 (0.58, 0.283)	3 (0.59, 0.280)	1 (0.31, 0.364)	1+ (0.43, 0.329)	1 (0.36, 0.350)	1+2 (0.40, 0.338)	+3+ (0.45, 0.322)	+3+ (0.62, 0.268)
7	1 (0.58, 0.361)	4 (0.60, 0.350)	2 (0.59, 0.357)	3 (0.60, 0.352)	1 (0.33, 0.453)	1+ (0.44, 0.413)	1 (0.38, 0.438)	1+2 (0.43, 0.417)	+3+ (0.47, 0.405)	+3+ -
8	1 (0.67, 0.279)	4 (0.68, 0.275)	2 (0.68, 0.277)	3 (0.68, 0.276)	1 (0.40, 0.376)	1+ (0.49, 0.348)	1 (0.44, 0.362)	1+2 (0.47, 0.355)	+3+ (0.51, 0.342)	+3+ (0.68, 0.273)
9	1 (0.44, 0.295)	2 (0.50, 0.281)	3 (0.50, 0.278)	4 (0.52, 0.274)	1 (0.17, 0.360)	1+ (0.31, 0.328)	1 (0.21, 0.351)	1+2 (0.31, 0.329)	+3+ (0.36, 0.316)	+3+ (0.60, 0.251)
10	1 (0.61, 0.326)	2 (0.62, 0.321)	4 (0.64, 0.315)	3 (0.63, 0.319)	1 (0.33, 0.426)	1+ (0.43, 0.392)	1 (0.37, 0.415)	1+2 (0.40, 0.402)	+3+ (0.46, 0.384)	+3+ (0.68, 0.297)
11	1 (0.52, 0.332)	2 (0.55, 0.319)	3 (0.56, 0.316)	4 (0.58, 0.308)	1 (0.23, 0.420)	1+ (0.38, 0.376)	1 (0.27, 0.407)	1+2 (0.34, 0.388)	+3+ (0.41, 0.365)	+3+ (0.62, 0.293)
12	1 (0.59, 0.366)	2 (0.60, 0.360)	3 (0.60, 0.357)	4 (0.62, 0.651)	1 (0.31, 0.470)	1+ (0.44, 0.426)	1 (0.36, 0.454)	1+2 (0.43, 0.431)	+3+ (0.46, 0.416)	+3+ (0.67, 0.327)
13	1 (0.49, 0.299)	2 (0.51, 0.293)	3 (0.52, 0.290)	4 (0.55, 0.283)	1 (0.24, 0.365)	1+ (0.39, 0.328)	1 (0.29, 0.355)	1+2 (0.38, 0.330)	+3+ (0.41, 0.322)	+3+ -
14	1 (0.54, 0.349)	2 (0.56, 0.341)	3 (0.56, 0.338)	4 (0.59, 0.328)	1 (0.27, 0.439)	1+ (0.41, 0.393)	1 (0.31, 0.427)	1+2 (0.39, 0.401)	+3+ (0.45, 0.381)	+3+ (0.65, 0.304)
15	1 (0.54, 0.349)	2 (0.56, 0.341)	3 (0.56, 0.339)	4 (0.59, 0.327)	1 (0.18, 0.447)	1+ (0.35, 0.397)	1 (0.22, 0.434)	1+2 (0.35, 0.397)	+3+ (0.42, 0.376)	+3+ (0.62, 0.305)
16	1 (0.45, 0.366)	2 (0.50, 0.350)	3 (0.51, 0.344)	4 (0.53, 0.336)	1 (0.27, 0.466)	1+ (0.40, 0.421)	1 (0.31, 0.453)	1+2 (0.41, 0.419)	3+ (0.45, 0.405)	+3+ (0.64, 0.327)

and timing between timeseries. The analysis of the T_s data suggested subtle spatial variability in T_s was primarily manifested in variability in diurnal T_s amplitude, which was principally controlled by variability in maximum T_s between sites.

Controls on temporal and spatial variability in near-surface debris temperature

To investigate whether meteorological conditions and site characteristics were associated with controlling T_s, and particularly maximum T_s, assessment of the influence of meteorological drives and site-specific traits was undertaken using multivariate analysis techniques.

Controls on temporal variability in near-surface debris temperature

Controls on temporal variability in T_s over the monsoon season were investigated for all hourly timeseries, omitting the period of sustained 0°C in T_s in which the debris surface was snow covered. Analysis was undertaken using stepwise multilinear regression (SMR), with meteorological timeseries as predictor variables, to determine the control and combined control of meteorological variables on T_s. SMR iteratively adds and removes variables included in the model based on their statistical significance in regression (Draper and Smith, 1998), therefore enabling the relative importance of meteorological variables to be identified. This method is superior to simply regressing individual variables against T_s as it can give insight into the extent to which different combinations of meteorological variables control T_s. Assessment of the meteorological data demonstrated that none of the timeseries were normally distributed, as for all T_s and T_a data. Consequently, to transform the T_s and meteorological variables to more approximately normal distributions, a simple natural logarithmic conversion was applied. The multivariate models described *T_s (where * reflects a log-transform) as a function of *SWin, *LWin, *T_{aG}, *RH (relative humidity) and *P (precipitation). The output from the primary SMR is detailed in Table VI highlighting the relative strength of the relationships between T_s and each of the meteorological variables between sites. *T_{aG} was ranked as the most influential predictor of *T_s for all sites, with coefficients of determination between R^2 = 0.44 and R^2 = 0.67. The addition of *SW_{in}, *LW_{in}, *RH and *P resulted in only minimal incremental increases in the strength of the correlation between predictor variables and *T_s, in all cases resulting in an increase in R^2 of ≤ 0.1. In all cases, *RH was only the third or fourth most significant predictor variable. *P was not significant in terms of contributing to improving prediction of *T_s for any site, and was therefore omitted from the model and not included in the first set of results (SMR1) in Table VI. Typically, the sites with the weakest SMR model were those classed as less representative of T_s, although Site 16 had similarly low results relative to all sites.

One of the potential weaknesses in the first pass SMR models is the collinearity between variables, particularly SW_{in} and T_a, for which r = 0.84 ($P << 0.05$). There is typically a positive relationship between incident solar radiation and T_a, due to the direct influence SW_{in} has on T_s (Hock, 2003), and the strong covariant relationship present between T_s and T_a (Foster *et al.*, 2012; Shaw *et al.*, 2016). Consequently, the SMR analyses were re-run with *T_{aG} removed from the model to explore whether additional variables influence T_s independent of T_{aG} (Table VI: SMR 2). Results highlighted that, in the absence of T_{aG}, all models exhibited *SW_{in} as the dominant predictor for T_s, but with coefficients of determination much reduced ($0.17 \leq R^2 \leq 0.40$). Inclusion of the other meteorological variables, while increasing the models' performance (with R^2 increasing to ≤0.49)

maintained less than 50% efficacy in predicting T_s (Table VI). Collinearity between P and RH, or between LW_{in} and RH may also be present but due to the minimal influence of these predictor variables on the SMR results identifying whether such collinearity existed here would be challenging, and so has not been considered further. Conflating the radiation terms (SW_{in} and LW_{in}) into 'net incident radiation' (NR_{in}) and continuing the omission of T_{aG} in a third set of SMR analyses (SMR 3) yielded similar results to SMR 2, with *NR_{in} being the dominant predictor variable; moreover, opting for inclusion of 'rate of change in T_{aG}' (dT_a) for the preceding hour, and cumulative radiation variables ($\sum SW_{in}$ and $\sum LW_{in}$) and 'time since precipitation' (tP) as potential drivers for T_s in SMR 3 showed similarly incremental improvements but only to $R^2 = 0.51$. In all cases in SMR 3, dT_a was the second most significant predictor variable. A final SMR model (SMR 4) excluded all radiation terms and utilised *RH, *P and tP. Despite the close association between incident radiation and T_a, the multivariate models using SW_{in}, LW_{in} and NR_{in} were less effective in describing T_s change over the monsoon season.

To gain a deeper understanding of the extent to which T_s and T_{aG} were related, and whether the two parameters have a varying temporal relationship, T_s and T_{aG} were also investigated for daytime (06:00–17:00) and night-time (18:00–05:00) periods separately. A number of previous studies have investigated the seasonal and diurnal variability of T_{aG} (Brock *et al.,* 2010; Steiner and Pellicciotti, 2015), and in some cases its relationship to T_s (Fujita and Sakai, 2000). As elsewhere, days when T_s was consistently 0°C (DOY 145–153) were excluded from the correlation analysis. The relationship between T_s and T_{aG} varied across the study period for both day and night (Figure 6). The relationship between T_s and T_{aG} was predominantly stronger at night ($r = 0.86$) than in the day ($r = 0.75$). Daytime T_s–T_{aG} correlations varied between $r = -0.01$ (DOY 190) and $r = 0.97$, while night-time correlations varied between $r = 0.48$ (DOY 188) and $r = 0.99$ (DOY 199). The seasonal and diurnal variation in the relationship between T_s and T_{aG} therefore suggests that T_{aG} was the dominant driver of T_s but that the strength of this relationship varied across a diurnal period and seasonally, due to diurnal and seasonal variation in additional incident or outgoing energy fluxes that also influence T_s.

Controls on spatial variability in near-surface debris temperature

To determine whether statistically significant relationships between site characteristics and between timeseries existed, as suggested by contrasting diurnal amplitudes and the lags between T_s timeseries, a two-step process of analysis was undertaken. Initially, stepwise generalised linear models (SGLMs) were explored to investigate possible controls on variability in T_s. SGLMs were undertaken rather than SMR due to the small sample size, and therefore the need to relax the assumptions of normal distribution of each timeseries. The SGLMs examined debris temperature metrics that included means for daily mean T_s, maximum T_s, minimum T_s and the daily mean amplitude of T_s for each site as the dependent variables. Site characteristics were used as predictor variables, including elevation, slope, aspect, mean clast size, lithology, terrain curvature and terrain roughness. A simple linear model was used, and potential interactions between site characteristics were not included. The less-representative timeseries (1, 2, 9, 11, 13) were omitted from the SGLMs, and 5% significance levels were used to eliminate weaker predictors. Second, following identification of the possible important predictor variables influencing T_s identified by the SGLM, linear bivariate regression (LBR) analysis was undertaken between T_s variables and the debris variables identified as important in the SGLMs. While the SGLM results give an insight into the combinations of debris characteristics that control the temperature variables, the LBR analysis enable the relationship between the predictor and T_s variables to be analysed in isolation.

Results of the SGLMs are given in Table VII, which includes variables that were identified as statistically significant in prediction of T_s. None of the models were improved through inclusion of site curvature or roughness, which may be due to the resolution of the DEM causing specific site metrics to be less than exact. The combination of clast size, lithology and slope played significant roles in the SGLMs, with coefficients of determination of around 0.9 for mean, maximum and amplitude T_s. Aspect was only considered important for predictions of minimum T_s, in which elevation was also critical. The LBR analysis results (Table VIII) show that the relationship between T_s variables and debris characteristics identified as influential in

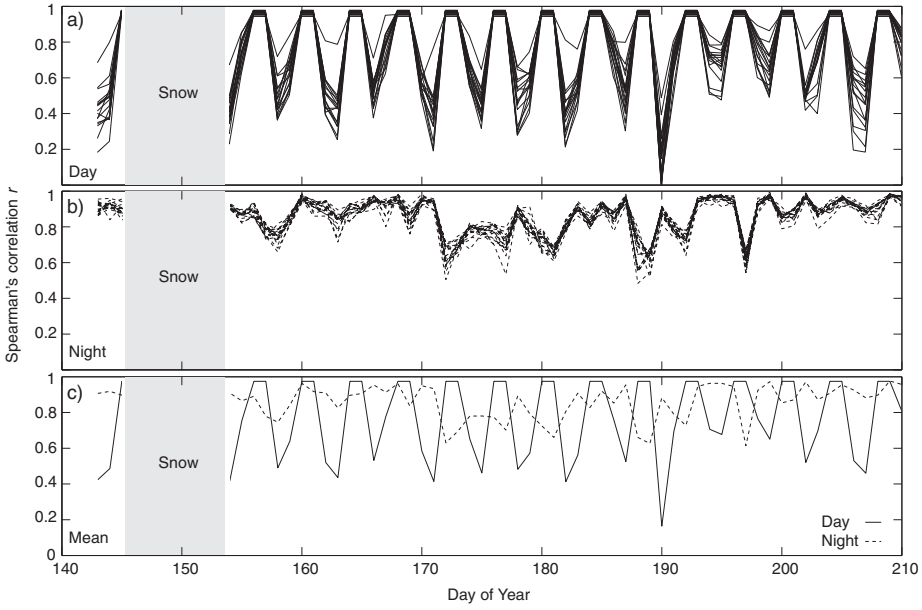

Figure 6. The correlation coefficient values (*r*) for the relationship between on-glacier air temperature (T_{aG}) and near-surface debris temperature (T_s), for (a) each daytime cycle (06:00–18:00) and (b) night-time cycle (18:00–06:00) over the study period; (c) presents the across-sites mean *r*-values for day and night.

Table VII. Stepwise generalised linear models (SGLMs) for describing debris temperature metrics based on environmental variables for the iButton sensor sites. Models detail the coefficients for each significant ($P < 0.05$) predictor variable, and summarise the model performance using the coefficient of determination and root mean square error (R^2, RMSE)

Ts metric	K (constant)	Elevation (m)	Clast size (m)	Lithology (% granite)	Slope (°)	Aspect (°)	R^2	RMSE
Min. T_s	–106.460	0.022				0.004	0.58	0.292
Mean T_s	19.590		–165.260	–0.111	0.259		0.82	0.514
Max. T_s	55.461		–566.370	–0.354	1.087		0.93	0.969
Amplitude T_s	50.819		–555.460	–0.342	1.185		0.93	0.992

Table VIII. Linear bivariate regression (LBR) analysis results (R^2) for debris metrics and debris characteristics for iButton sensor sites, excluding the less representative sites. All P values were >0.05 and so were not statistically significant, except for minimum T_s and elevation ($P = 0.02$)

Ts metric	Elevation (m)	Clast size (m)	Lithology (% granite)	Slope (°)	Aspect (°)
Min. T_s	0.44				0.01
Mean T_s		0.05	<0.01	0.05	
Max. T_s		0.07	<0.01	0.10	
Amplitude T_s		0.07	<0.01	0.12	

the SGLMs were not statistically significant in isolation. The exception was minimum T_s and elevation, which had an R^2 of 0.44 ($P = 0.02$).

Consequently, although clast size, lithology and slope influence T_s metrics in conjunction with one another, they have little influence on T_s independently. Specifically, debris size and lithology are considered to have an impact on the absorption and transfer of solar radiation through a debris layer through their influence on albedo, porosity and moisture content, while slope is a critical factor influencing solar radiation receipt. The southerly aspect of the majority of the sites reported here may undermine identification of the merit in describing T_s metrics using aspect. In addition, the lack of prediction of minimum T_s by the debris variables except for elevation suggests that minimum T_s may be independent of the majority of variables considered, but may be most appropriate for identification using a lapse rate. While the sample set was relatively small, the SGLMs illustrated the potential for physical site characteristics to modulate T_s, the importance of considering a suite of debris characteristics and their combined influence in control of T_s.

Discussion

The timeseries analyses detailed above identified a number of key aspects in the variability in T_s for thick (>1 m) debris on the debris-covered ablation area of Khumbu Glacier. A seasonal trend of decreasing maximum and mean T_s was identified at the majority of sites, while an increase in minimum T_s was in contrast to seasonal changes in T_a. A systematic shift from a dominant smooth diurnal cycle in T_s early in the monsoon season to a lagged cycle as the monsoon progressed occurred, alongside which meteorological conditions became more varied. In terms of spatial contrasts, there was evidence of subtle differences between sites, illustrated by disparities in how closely the T_s timeseries paralleled each other, and short term (≤2 h) lags in T_s between sites. Exploring these differences through consideration of meteorological drivers and potential site characteristic controls enabled identification of a dominant association between T_a and T_s and the influential role of clast size, lithology and slope on T_s metrics at each site. Here, we discuss the processes that may underlie the observed variability in T_s on a debris-covered glacier.

Temporal variability in near-surface debris temperature

The near-surface debris temperature (T_s) timeseries were notably perturbed between DOY 145 and 153, during which a period of sustained 0°C occurred following an observed major snowfall event. Following the period of 0°C, short-term variability on timescales of around 3–8 days and a seasonal trend in decreasing maximum T_s were observed in all T_s timeseries. The timing of short-term variability in T_s and SW_{in}, LW_{in}, RH and precipitation was simultaneous, while the seasonal decrease in maximum T_s occurred alongside a trend of decreasing SW_{in}, increasing T_a, LW_{in} and RH, and increased frequency of precipitation (Figure 3). The coincidence of the seasonal trends in meteorological variables provide a strong indication of increased cloudiness over the study period (Mölg *et al.,* 2009; Sicart *et al.,* 2006; Van Den Broeke *et al.,* 2006).

Increasing cloud cover results in a decreasing amount of SW_{in} reaching the debris surface, causing maximum T_s to decrease, which occurs in all timeseries presented here, and a delay in the time at which maximum T_s is achieved as the incoming energy flux to the debris surface is reduced and the debris therefore takes longer to heat up. Consequently, such an increase in cloudiness over the study period would have resulted in the decrease in the diurnal amplitude of T_s, and a delay in the timing of peak diurnal T_s, both of which are observed in changing modes of variation in T_s identified in the PCA (Figure 4). An additional control on decreasing SW_{in} would be that following midsummer (DOY 172) regional SW_{in} and solar angle would decrease, reducing the intensity and duration of SW_{in} a debris surface would receive. However, the decrease in SW_{in} was initiated before DOY 172, suggesting this trend was primarily dependent on increasing cloud cover.

A seasonal increase in cloud cover, relative humidity and the frequency of precipitation would also increase the moisture content of the debris layer. Moisture content of the debris layer has the potential to affect T_s considerably (Collier *et al.,* 2014), but is challenging to quantify and not reported here. The presence of moisture in a debris layer affects its effective thermal conductivity and therefore the energy needed to increase bulk temperature. An increased amount of energy would therefore be needed to heat water-filled pores to the same temperature as air-filled pores within the debris layer (Collier *et al.,* 2014; Evatt *et al.,* 2015). Consequently, as incoming energy to the

debris surface decreased during the monsoon season, and the amount of energy needed to maintain debris layer temperature would increase due to presence of moisture-filled rather than air-filled pores, and mean T_s would decrease. In addition, an increasingly moist debris layer would have decreased T_s due to enhanced latent heat exchange and subsequent loss of heat through evaporation in the debris surface layer (Cuffey and Paterson, 2010; Takeuchi *et al.,* 2000). These trends in T_s are observed in the timeseries presented here, and alongside the precipitation timeseries, suggest debris moisture content may have been a factor in controlling T_s. However, direct collection of data for moisture content is needed to confirm the link between T_s and debris moisture content.

While the 1–3 day cycles are considered to be the passing of localised weather systems in the Khumbu valley, the 5–8 day cyclic perturbations of T_s were synchronous with periods of markedly lower SW_{in}, higher LW_{in} and relative humidity, and higher P. These perturbations suggest the intensity of cloud cover was also temporally variable, resulting in periods of T_s with decreased diurnal amplitude and lower maximum T_s. The perturbations of T_s were increasingly frequent in the latter half of the study period, evidenced by the majority of days loaded to PC2 present in this period. These perturbations suggest that alongside seasonal increase in cloud cover due to progression of the monsoon, more localised weather patterns still contribute to variability in meteorological parameters that also affect T_s.

Spatial variability in near-surface debris temperature

Despite the period of asynchronous snow melt and subsequent spatial variation in T_s between sites for the period DOY 145–153, all T_s data displayed strong similarity for the majority of the study period, evidenced in the *r* and *E* values for the raw data and the *r* values for the detrended timeseries. *E* values suggested subtle variability did exist between sites, which was primarily manifested in the amplitude and magnitude of temperature recorded at each site rather than the pattern of T_s.

Variability in sensor depth may have caused some variability in *E* between site pairs. Although sensor depth variability was accounted for using the temperature gradient through a debris layer, which was calculated by Nicholson and Benn (2006), their gradients were means of a day (24 h) period. As mentioned previously, applying a daily gradient to determine uncertainty in T_s due to depth does not reflect the diurnal variability of temperature with depth, which would affect the magnitude and pattern of T_s recorded between sites (Nicholson and Benn 2006). However, after the sites identified as less representative of T_s were omitted, sensor depth varied by <0.03 m, which would have produced a maximum uncertainty of 0.44°C between sites (excluding less representative sites) even for the steepest gradients previously identified (at 13:00 by Nicholson and Benn 2006). Variability of T_s between sites reached 10°C throughout the study period, which exceeds discrepancies exclusively due to sensor depth and so instead suggests other drivers of spatial variability in T_s between sites.

Controls on variability in near-surface debris temperature

Coincident trends in T_s and meteorological variables suggest a high level of interconnection between meteorological variables and T_s. T_{aG} explained the majority of the relationship identified between meteorological variables and T_s through SMR for all sites (Petersen *et al.,* 2013), while the other meteorological variables identified to be statistically significant in the SMR1 model (SW_{in}, LW_{in} and RH) were less effective as predictors (Table VI). Omission of T_{aG} in SMR models identified SW_{in}, LW_{in} and RH as contributory drivers of T_s, and thus reiterates the complexity of the energy balance at a debris-covered surface where all of the meteorological parameters play some role in controlling T_s. However, within the SMR models, the strongest relationship between T_{aG} and T_s was $R^2 = 0.67$, and inclusion of additional variables only improved model performance to a maximum R^2 of 0.68 (Table VI), suggesting T_{aG} is the most important driver of T_s, and that temperature-index melt models that calculate T_s from T_{aG} will account for at least two-thirds of temporal variability in energy input to the debris surface. Consequently, these results suggest that when debris surface temperature is being modelled at a daily time step, a temperature-index model using only the relationship between T_{aG} and T_s is considered appropriate, as the incorporation of additional parameters such as SW_{in} and NR_{in} would provide minimal improvement in model performance. However, variation in the relationship between T_{aG} and T_s over a diurnal cycle (e.g. Figure 6) suggests the strength of this relationship would be less applicable when modelling T_s on sub-daily time steps.

Unravelling the relationship between T_{aG} and T_s is complex, as the two variables are interdependent on one another (Shaw *et al.,* 2016), particularly when T_a is collected below the standard height of 2 m above the glacier surface in the surface boundary layer (Reid *et al.,* 2012; Wagnon *et al.,* 1999). Critically, here, T_{aP} and T_{aG} were highly correlated ($r = 0.72$, $P < 0.05$), but accounting for the elevation difference using a lapse rate of –0.0046°C m^{-1} appropriate for the monsoon season on Khumbu Glacier (Shea *et al.,* 2015) and a standard lapse rate of –0.0065°C m^{-1}, exhibited mean residuals between T_{aP} and T_{aG} of –1.9°C and –1.3°C, evidencing the observation that T_{aG} was consistently significantly higher than T_{aP}. This on-/off-glacier contrast is due to heat loss from the thick supraglacial debris layer to the near-surface atmosphere through turbulent heat exchange (Takeuchi *et al.,* 2000). Our results mirror those of Steiner and Pellicciotti (2015) where T_{aP} from equivalent elevations was consistently lower than T_{aG} over a debris-covered surface, highlighting the need to use off-glacier temperature records with caution when driving numerical models of glacier ablation, and wherever possible use on-glacier measurements.

The influence of specific meteorological controls of T_s was also spatially variable (Table VI). Although a difference in elevation between the T_s sensors and the T_a sensor existed, variability in the relationship between T_{aG} and T_s is predominately attributed to spatial variability between the sites at which T_s was recorded. The maximum elevation variation between T_s and T_{aG} sensors was 47 m, which, using the range of lapse rates described above, would result in variations in T_{aG} of up to 0.3°C across the study site, which is below the T_{aG} sensor uncertainty. Differences between T_a and T_s were greater than 0.3°C for all sites. The spatial variability in T_s is therefore attributed to variation in a combination of slope, lithology and clast size between sites, variables found to be important for variability in maximum T_s between sites, which would result in varying effective thermal conductivity between sites.

The results of the SGLM analysis support previous work on debris-free and debris-covered glaciers, and in permafrost environments, where topographic controls including aspect, slope (Gao *et al.,* 2017; Gubler *et al.,* 2011; Guglielmin *et al.,* 2012; Hock and Holmgren, 1996; Strasser *et al.,* 2004), albedo and surface roughness (considered a factor due to the importance of clast size; Brock *et al.,* 2000; Mölg and Hardy, 2004) were found to influence spatial variability in the incoming energy flux to the ground surface, and would therefore be

anticipated to control T_s. The most dominant variables describing T_s metrics from each site on Khumbu Glacier were slope, clast size and lithology. These variables would be expected to control incident radiation receipt through solar geometry and albedo, moisture content and evaporation, and affect local thermal conductance. However, these debris properties were only found to influence T_s metrics in conjunction with one another and were not found to independently control T_s. Without further data such as site-specific moisture content and SW_{in} values for each site, the exact controls on such variability cannot be identified. In addition, elevation and aspect were only found to influence minimum T_s. The majority of sites reported here were south facing and therefore provide a systematic bias, hindering ultimate identification of the influence of this variable. However, the relatively strong, and statistically significant, relationship between the elevation and minimum T_s suggests estimation of minimum T_s using lapse rates, and potentially night time temperatures when T_s is at its minimum, to estimate spatial variability in T_s would be appropriate.

The diurnal and seasonal variability in the relationship between T_{aG} and T_s identified here builds on the conclusions of Steiner and Pellicciotti (2015), who identified a variation in relationship between the two parameters between night and day and with differing climatic conditions. The occurrence of a seasonal influence in this variable relationship is attributed to variability in meteorological parameters, with decreased strength of the relationship between T_{aG} and T_s occurring concurrently with perturbations in SW_{in}, and peaks in LW_{in} and RH (e.g. around DOY 173). Such variability is attributed to differences in the capacity of air and debris to hold thermal energy, and the addition of moisture in either or both environments, causing the relationship to vary between T_{aG} and T_s seasonally as well as diurnally. Understanding the importance of the high RH values and precipitation is also important for understanding the effect of turbulent heat flux on glacier ablation for these monsoon-influenced debris-covered glaciers (Suzuki *et al.,* 2007). The correlation coefficients for the T_s–T_{aG} relationship presented here also reinforce the findings of Steiner and Pellicciotti (2015), displaying stronger relationships at night due to T_s increasing at a greater rate and magnitude than T_{aG}. Consequently, temperature-index melt models with a sub-daily time, which rely on the relationship between T_{aG} and T_s, need to consider additional controls on T_s such as diurnal and seasonal fluctuations in incoming radiative fluxes, particularly for monsoon-influenced debris-covered glaciers that experience large variability in seasonal weather patterns. However, further investigation into the relationship between meteorological variables, T_{aG} and T_s over diurnal cycles is needed to quantify the relative influence of radiative fluxes on T_s.

Implications of variability in near-surface debris temperature

While the results of this study provide an interesting insight into the extent of temporal and spatial variability in T_s for thick (>1 m) supraglacial debris layers, there is a need to carry out a similar study on thinner debris layers as debris-covered glaciers exist in a range of climatic conditions. Following such studies, a development of surface energy balance models to incorporate spatiotemporal variations in debris properties would be appropriate for modelling mass balance, and also for constraining surface energy balance models used for estimating debris thickness (Foster *et al.,* 2012; Rounce and McKinney, 2014). Our findings advocate the use of a surface energy balance approach for calculating debris layer thickness rather than a direct empirical relationship between T_s and debris layer thickness as used by Mihalcea *et al.* (2008a, 2008b) and Minora *et al.* (2015). The latter of these approaches oversimplifies the relationship between T_s and debris thickness, and omits additional factors such as the influential relationship between SW_{in} and T_s, and spatial variability of T_s due to varying slope, lithology and clast size of the debris layer. This study suggests that inclusion of site characteristics such as slope and aspect and debris characteristics such as moisture content, porosity, lithology and thermal conductivity would increase the accuracy of results using the surface energy balance approach. Further investigation into the extent of spatial variations in site and debris properties on a glacier scale and the influence of these characteristics on debris surface temperature is therefore needed to constrain such model development. In the meantime, application of either method for estimation of debris thickness (empirical and energy-balanced methods) should acknowledge the possible uncertainty involved in disregarding spatial variability in debris properties and compare their debris thickness estimates with direct field measurements of debris thickness. For energy balance models that calculate glacier mass balance, temporal variation in debris properties, specifically moisture content, have the potential to influence energy exchange at a supraglacial debris surface and through a debris layer, and therefore ablation that occurs under a supraglacial debris layer. However, as highlighted in this study, little is known about such temporal variation in debris properties and so constraining this variability should be the focus of future investigations into supraglacial debris properties.

Conclusions

This study presents the most comprehensive analysis of near-surface debris temperature (T_s) data for a Himalayan debris-covered glacier to date. The timeseries presented extend beyond describing the influence of debris layer thickness on near-surface debris temperature, and confirm both temporal and spatial variability in T_s on Khumbu Glacier. Sixteen sites across Khumbu Glacier's debris-covered ablation area displayed a marked daily cycle in T_s, overlying seasonal, short-term and spatial variation in maximum T_s and diurnal amplitude. A clear transition in the mode of diurnal variation was associated with increasing cloud cover and precipitation; the latter considered to control debris moisture content. Differences in the magnitude and range of variation in T_s were apparent between sites, and were indicative of contrasts in response of T_s to meteorological or environmental variables. A close association between on-glacier air temperature (T_{aG}) and T_s was evident while radiative energy had a lesser influence on T_s. Analyses of these timeseries also demonstrated the role that the site characteristics slope, lithology and clast size hold in controlling spatial variability in T_s when in conjunction with one another, but have little controlling influence on spatial variability of maximum T_s in isolation, and that minimum T_s is influenced by elevation and aspect. Consequently, this study specifically identified the variables controlling temporal and spatial variability in T_s for debris-covered glacier surface with a debris layer thickness of over 1 m.

Our results reinforce the complexity and interconnected nature of the surface energy balance at a supraglacial debris surface, identifying that energy fluxes such as ambient air temperature and incoming radiative flux at the debris surface, as well as debris characteristics such as lithology and clast size to a degree, regulate debris surface temperature but are not independent of one another. Hence, these results suggest that, although temperature-index melt models can be useful for

estimating supraglacial debris thickness or ablation for daily time steps, these models should follow an enhanced approach in which additional aspects of energy exchange such as incoming solar radiation are included when modelling at a sub-daily (e.g. hourly) resolution (Carenzo *et al.*, 2016). These models also need to consider spatial and temporal variation in the controlling variables used (e.g. air temperature and incoming solar radiation), and use on-glacier air temperature to reduce uncertainties in estimates of ablation. Studies that simulate ablation or derive debris thickness should consider including spatial variability in T_s and debris thickness in model calibrations, and consider the influence of variability in site characteristics on these results, in particular with regards to their influence on bulk effective thermal conductivity of the debris layer. Finally, the data presented here were limited to debris layers >1 m thick, and future studies should assess the role of debris characteristics and local topography in defining the energy exchange and T_s across thinner debris layers to enable the variability of and controls on surface temperature to be understood across an entire debris-covered glacier surface.

Acknowledgements—Fieldwork was funded by the British Society for Geomorphology and a Royal Society (Research Grant RG120393 to AVR and DJQ). Thank you to our Nepalese guides, Karma, Karma Tindu and Rajesh for their invaluable help during fieldwork. Also thanks to Dr P. Porter, University of Hertfordshire for the loan of field equipment and Owen King for the use of the corrected SETSM DEM. We thank the anonymous reviewers for their constructive and thorough comments that have much improved this manuscript.

References

Ageta Y. 1976. Characteristics of precipitation during monsoon season in Khumbu Himal. *Journal of the Japanese Society of Snow and Ice* **38**: 84–88. https://doi.org/10.5331/seppyo. 38.Special_84.

Apaloo J, Brenning A, Bodin X. 2012. Interactions between seasonal snow cover, ground surface temperature and topography (Andes of Santiago, Chile, 33.5°S). *Permafrost and Periglacial Processes* **23**: 277–291. https://doi.org/10.1002/ppp.1753.

Arendt A, Bolch T, Cogley JG, Gardner A, Hagen JO, Hock R, Kaser G, Pfeffer WT, Moholdt G, Paul F, Radic V. 2012. *Randolph Glacier Inventory [v2. 0]: A Dataset of Global Glacier Outlines, Global Land Ice Measurements from Space*, Boulder Colorado, USA.

Benn DI, Lehmkuhl F. 2000. Mass balance and equilibrium-line altitudes of glaciers in high-mountain environments. *Quaternary International* **65–66**: 15–29. https://doi.org/10.1016/S1040-6182(99)00034-8.

Bolch T, Buchroithner M, Pieczonka T, Kunert A. 2008. Planimetric and volumetric glacier changes in the Khumbu Himal, Nepal, since 1962 using Corona, Landsat TM and ASTER data. *Journal of Glaciology* **54**: 592–600.

Bolch T, Pieczonka T, Benn DI. 2011. Multi-decadal mass loss of glaciers in the Everest area (Nepal Himalaya) derived from stereo imagery. *The Cryosphere* **5**: 349–358.

Bollasina M, Bertolani L, Tartari G. 2002. Meteorological observations at high altitude in the Khumbu Valley, Nepal Himalayas, 1994–1999. *Bulletin of Glaciological Research* **19**: 1–11.

Bookhagen B, Burbank DW. 2010. Toward a complete Himalayan hydrological budget: spatiotemporal distribution of snowmelt and rainfall and their impact on river discharge. *Journal of Geophysical Research* **115**: F03019–F03025. https://doi.org/10.1029/2009JF001426.

Borradaile GJ. 2013. *Statistics of Earth Science Data: their Distribution in Time, Space and Orientiation*. Springer Science and Business Media: London.

Brazel AJ, Chambers FB, Kalkstein LS. 1992. Summer energy balance on West Gulkana Glacier, Alaska, and linkages to a temporal synoptic index. *Zeitschrift fur Geomorphologie* **86**: 15–34.

Brock BW, Mihalcea C, Kirkbride MP, Diolaiuti G, Cutler MEJ, Smiraglia C. 2010. Meteorology and surface energy fluxes in the 2005–2007 ablation seasons at the Miage debris−covered glacier, Mont Blanc Massif, Italian Alps. *Journal of Geophysical Research: Atmospheres* **115**: 112. https://doi.org/10.1029/2009JD013224.

Brock BW, Willis IC, Sharp MJ, Arnold NS. 2000. Modelling seasonal and spatial variations in the surface energy balance of Haut Glacier d'Arolla, Switzerland. *Annals of Glaciology* **31**: 53–62. https://doi.org/10.3189/172756400781820183.

Carenzo M, Pellicciotti F, Mabillard J, Reid T, Brock BW. 2016. An enhanced temperature idnex model for debris-covered glaciers accounting for thickness effect. *Advances in Water Resources* **94**: 457–469.

Clark DH, Clark MM, Gillespie AR. 1994. Debris-covered glaciers in the Sierra Nevada, California, and their implications for snowline reconstructions. *Quaternary Research* **41**: 139–153. https://doi.org/10.1006/qres. 1994.1016.

Collier E, Nicholson LI, Brock BW, Maussion F, Essery R, Bush ABG. 2014. Representing moisture fluxes and phase changes in glacier debris cover using a reservoir approach. *The Cryosphere* **8**: 1429–1444. https://doi.org/10.5194/tc-8-1429-2014.

Conway H, Rasmussen LA. 2000. Summer temperature profiles within supraglacial debris on Khumbu Galcier, Nepal. In *Debris-covered Glaciers: Proceedings of an international workshop held at the University of Washington*, Vol. **264**: Seattle: Washington, USA; 89–97.

Cuffey KM, Paterson WS. 2010. *The Physics of Glaciers*. Elsevier: London, UK.

Davis RE, Kalkstein LS. 1990. Development of an automated spatial synoptic climatological classification. *International Journal of Climatology* **10**: 769–794.

Draper NR, Smith H. 1998. *Applied Regression Analysis*. Wiley-Interscience: New Jersey.

Evatt GW, Abrahams ID, Heil M, Mayer C, Kingslake J, Mitchell SL, Fowler AC, Clark CD. 2015. Glacial melt under a porous debris layer. *Journal of Glaciology* **61**: 825–836. https://doi.org/10.3189/2015JoG14J235.

Foster LA, Brock BW, Cutler MEJ, Diotri F. 2012. A physically based method for estimating supraglacial debris thickness from thermal band remote-sensing data. *Journal of Glaciology* **58**: 677–691. https://doi.org/10.3189/2012JoG11J194.

Fujita K, Sakai A. 2000. Air temperature environment on the debris-covered area of Lirung Glacier, Langtang Valley, Nepal Himalayas. In *Debris-covered Glaicers: Proceedings of an international workshop held at the University of Washington*, Vol. 264: Seattle, Washington, USA; 83–88.

Gades A, Conway H, Nereson N, Naito N, Kadota T. 2000. Radio echo-sounding through supraglacial debris on Lirung and Khumbu Glaciers, Nepal Himalayas. In *Debris-Covered Glaciers: Proceedings of an International Workshop held at the University of Washington*, Vol. **264**: Seattle, Washington, USA; 13–24.

Gao H, Ding Y, Zhao Q, Hrachowitz M, Savenije HHG. 2017. The importance of aspect for modelling the hydrological response in a glacier catchment in Central Asia. *Hydrological Processes*. https://doi.org/10.1002/hyp. 11224.

Gisnås K, Westermann S, Schuler TV, Litherland T, Isaksen K, Boike J, Etzelmüller B. 2014. A statistical approach to represent small-scale variability of permafrost temperatures due to snow cover. *The Cryosphere* **8**: 2063–2074. https://doi.org/10.5194/tc-8-2063-2014.

Glasser NF, Holt TO, Evans ZD, Davies BJ, Pelto M, Harrison S. 2016. Recent spatial and temporal variations in debris cover on Patagonian glaciers. *Geomorphology* **273**: 202–216. https://doi.org/10.1016/j.geomorph. 2016.07.036.

Gubler S, Fiddes J, Keller M, Gruber S. 2011. Scale-dependent measurement and analysis of ground surface temperature variability in alpine terrain. *The Cryosphere* **5**: 431–443. https://doi.org/10.5194/tc-431-2011.

Guglielmin M. 2006. Ground surface temperature (GST), active layer and permafrost monitoring in continental Antarctica. *Permafrost and Periglacial Processes* **17**: 133–143. https://doi.org/10.1002/ppp. 553.

Guglielmin M, Worland MR, Cannone N. 2012. Spatial and temporal variability of ground surface temperature and active layer thickness at the margin of maritime Antarctica, Signy Island. *Geomorphology* **155–156**: 20–33.

Hambrey MJ, Quincey DJ, Glasser NF, Reynolds JM, Richardson SJ, Clemmens S. 2008. Sedimentological, geomorphological and dynamic context of debris-mantled glaciers, Mount Everest

(Sagarmatha) region, Nepal. *Quaternary Science Reviews* **27**: 2361–2389. https://doi.org/10.1016/j.quascirev. 2008.08.010.
Hannah DM, Smith BP, Gurnell AM, McGregor GR. 2000. An approach to hydrograph classification. *Hydrological Processes* **14**: 317–338.
Hock R. 2003. Temperature index melt modelling in mountain areas. *Journal of Hydrology* **282**: 104–115.
Hock R, Holmgren B. 1996. Some aspects of energy balance and ablation of Storglaciaren, Northern Sweden. *Geografiska Annaler: Series A, Physical Geography* **78**: 121.
Hubbart J, Link T, Campbell C, Cobos D. 2005. Evaluation of a low−cost temperature measurement system for environmental applications. *Hydrological Processes* **19**(7): 1517–1523.
Igathinathane C, Pordesimo LO, Columbus EP, Batchelor WD, Sokhansanj S. 2009. Sieveless particle size distribution analysis of particulate materials through computer vision. *Computers and Electronics in Agriculture* **66**: 147–158.
Inoue J. 1977. Mass budget of Khumbu glacier. *Journal of the Japanese Society of Snow and Ice* **39**: 15–19. https://doi.org/10.5331/seppyo. 39.Special_15.
Irvine-Fynn TDL, Moorman BJ, Willis IC, Sjogren DB, Hodson AJ, Mumford PN, Walter FSA, Williams JLM. 2005. Geocryological processes linked to High Arctic proglacial stream suspended sediment dynamics: examples from Bylot Island, Nunavut, and Spitsbergen, Svalbard. *Hydrological Processes* **19**: 115–135. https://doi.org/10.1002/hyp. 5759.
Iwata S, Watanabe O, Fushimi H. 1980. Surface morphology in the ablation area of the Khumbu glacier. *Journal of the Japanese Society of Snow and Ice* **41**: 9–17. https://doi.org/10.5331/seppyo. 41.-special_9.
Jansson P, Fredin O. 2002. Ice sheet growth under dirty conditions: implications of debris cover for early glaciation advances. *Quaternary International* **95–96**: 35–42. https://doi.org/10.1016/S1040-6182(02)00025-3.
Kadota T, Seko K, Aoki T, Iwata S. 2000. Shrinkage of the Khumbu Glacier, east Nepal from 1978 to 1995. In *Debris-covered Glaciers: Proceedings of an international workshop held at the University of Washington*, Vol. **264**: Seattle, Washington, USA; 235–244.
King O, Quincey DJ, Carrivick JL, Rowan AV. 2017. Spatial variability in mass loss of glaciers in the Everest region, central Himalayas, between 2000 and 2015. *The Cryosphere* **11**: 407–426.
Kirkbride MP. 2000. Ice-marginal geomorphology and Holocene expansion of debris-covered Tasman Glacier, New Zealand. In *Debris-covered Glaciers: Proceedings of an international workshop held at the University of Washington*, Vol. **264**: Seattle, Washington, USA; 211–218.
Kirkbride MP. 2011. Debris-covered glaciers. In *Encyclopaedia of Snow, Ice and Glaciers*. Springer: New York; 180–182.
Krause P, Boyle DP, Bäse F. 2005. Comparison of different efficiency criteria for hydrological model assessment. *Advances in Geosciences* **5**: 89–97.
Kristoufek L. 2014. Detrending moving-average cross-correlation coefficient: measuring cross-correlations between non-stationary series. *Physical A: Statistical Mechanics and its Applications* **406**: 169–175.
Legates DR, McCabe GJ. 1999. Evaluating the use of 'goodness−of−fit' measures in hydrologic and hydroclimatic model validation. *Water Resources Research* **35**: 233–241. https://doi.org/10.1029/1998WR900018.
Lewkowicz AG. 2008. Evaluation of miniature temperature-loggers to monitor snowpack evolution at mountain permafrost sites, northwestern Canada. *Permafrost and Periglacial Processes* **19**(3): 323–331.
Lundquist JD, Cayan DR. 2007. Surface temperature patterns in complex terrain: daily variations and long−term change in the central Sierra Nevada, California. *Journal of Geophysical Research: Atmospheres* **112**(D11): 124. https://doi.org/10.1029/2006JD007561.
Mattson LE. 2000. The influence of a debris cover on the mid-summer discharge of Dome Glacier, Canadian Rocky Mountains. In *Debris-covered Glaciers: Proceedings of an international workshop held at the University of Washington. Seattl: Washington, USA* **264**: 25–34.
Mihalcea C, Mayer C, Diolaiuti G, D'Agata C, Smiraglia C, Lambrecht A, Vuillermoz E, Tartari G. 2008a. Spatial distribution of debris thickness and melting from remote-sensing and meteorological data, at debris-covered Baltoro glacier, Karakoram, Pakistan. *Annals of Glaciology* **48**: 49–57. https://doi.org/10.3189/172756408784700680.
Mihalcea C, Brock BW, Diolaiuti G, D'Agata C, Citterio M, Kirkbride MP, Cutler MEJ, Smiraglia C. 2008b. Using ASTER satellite and ground-based surface temperature measurements to derive supraglacial debris cover and thickness patterns on Miage Glacier (Mont Blanc Massif, Italy). *Cold Regions Science and Technology* **52**: 341–354.
Mihalcea C, Mayer C, Diolaiuti G, Lambrecht A, Smiraglia C, Tartari G. 2006. Ice ablation and meteorological conditions on the debris-covered area of Baltoro glacier, Karakoram, Pakistan. *Annals of Glaciology* **43**: 292–300. https://doi.org/10.3189/172756406781812104.
Minder JR, Mote PW, Lundquist JD. 2010. Surface temerpature lapse rates over complex terrain: lessons from the Cascade Mountains. *Journal of Geophysical Research: Atmosphere* **115**: 1–13.
Minora U, Senese A, Bocchiola D, Soncini A, D'agata C, Ambrosini R, Mayer C, Lambrecht A, Vuillermoz E, Smiraglia C, Diolaiuti G. 2015. A simple model to evaluate ice melt over the ablation area of glaciers in the Central Karakoram National Park, Pakistan. *Annals of Glaciology* **56**: 202–216.
Mölg T, Cullen NJ, Kaser G. 2009. Solar radiation, cloudiness and longwave radiation over low-latitude glaciers: implications for mass-balance modelling. *Journal of Glaciology* **55**: 292–302. https://doi.org/10.3189/002214309788608822.
Mölg T, Hardy DR. 2004. Ablation and associated energy balance of a horizontal glacier surface on Kilimanjaro. *Journal of Geophysical Research: Atmospheres* **109**: 159. https://doi.org/10.1029/2003JD004338.
Nakawo M, Rana B. 1999. Estimate of ablation rate of glacier ice under a supraglacial debris layer. *Geografiska Annaler: Series A, Physical Geography* **81**: 695–701. https://doi.org/10.1111/1468-0459.00097.
Nakawo M, Young GJ. 1981. Field experiments to determine the effect of a debris layer on ablation of glacier ice. *Annals of Glaciology* **2**: 85–91. https://doi.org/10.3189/172756481794352432.
Nakawo M, Young GJ. 1982. Estimate of glacier ablation under a debris layer from surface temperature and meteorological variables. *Journal of Glaciology* **28**: 29–34.
Nayava JL. 1974. Heavy monsoon rainfall in Nepal. *Weather* **29**: 443–450. https://doi.org/10.1002/j.1477-8696.1974.tb03299.x.
Nicholson L, Benn DI. 2006. Calculating ice melt beneath a debris layer using meteorological data. *Journal of Glaciology* **52**: 463–470. https://doi.org/10.3189/172756506781828584.
Nicholson L, Benn DI. 2013. Properties of natural supraglacial debris in relation to modelling sub-debris ice ablation. *Earth Surface Processes and Landforms* **28**: 490–501.
Noh MJ, Howat IM. 2015. Automated stereo-photogrammetric DEM generation at high latitudes: surface extraction with TIN-based search-space minimization (SETSM) validation and demonstration over glaciated regions. *GIScience and Remote Sensing* **52**: 198–217. https://doi.org/10.1080/15481603.2015.1008621.
Nuimura T, Fujita K, Fukui K, Asahi K, Aryal R, Ageta Y. 2011. Temporal changes in elevation of the debris-covered ablation area of Khumbu Glacier in the Nepal Himalaya since 1978. *Arctic, Antarctic and Alpine Research* **43**: 246–255. https://doi.org/10.1657/1938-4246-43.2.246.
Østrem G. 1959. Ice melting under a thin layer of moraine, and the existence of ice cores in moraine ridges. *Geografiska Annaler* **41**: 228–230. https://doi.org/10.2307/4626805.
Petersen L, Pellicciotti F, Juszak I, Carenzo M, Brock B. 2013. Suitability of a constant air temperature lapse rate over an Alpine glacier: testing the Greuell and Böhm model as an alternative. *Annals of Glaciology* **54**: 120–130. https://doi.org/10.3189/2013AoG63A477.
Quincey DJ, Luckman A, Benn DI. 2009. Quantification of Everest region glacier velocities between 1992 and 2002, using satellite radar interferometry and feature tracking. *Journal of Glaciology* **55**: 596–605.
Rasband WS. 2008. *ImageJ* [online] Available from: http://rsbweb.nih.gov/ij/
Reid TD, Carenzo M, Pellicciotti F, Brock BW. 2012. Including debris cover effects in a distributed model of glacier ablation. *Journal of Geophysical Research: Atmospheres*: 117. https://doi.org/10.1029/2012JD017795.
Reznichenko N, Davies T, Shulmeister J, McSaveney M. 2010. Effects of debris on ice-surface melting rates: an experimental study. *Journal of Glaciology* **56**: 384–394. https://doi.org/10.3189/002214310792447725.

Romanovsky VE, Osterkamp TE. 2000. Effects of unfrozen water on heat and mass transport processes in the active layer and permafrost. *Permafrost and Periglacial Processes* **11**: 219–239. https://doi.org/10.1002/1099-1530(200007/09)11:3<219::AID-PPP352>3.0.CO;2-7.

Rounce DR, McKinney DC. 2014. Debris thickness of glaciers in the Everest area (Nepal Himalaya) derived from satellite imagery using a nonlinear energy balance model. *The Cryosphere* **8**: 1317–1329. https://doi.org/10.5194/tc-8-1317-2014.

Rounce DR, Quincey DJ, McKinney DC. 2015. Debris-covered glacier energy balance model for Imja-Lhotse Shar Glacier in the Everest Region of Nepal. *The Cryosphere* **9**: 2295–2310. https://doi.org/10.5194/tc-9-2295-2015.

Roznik EA, Alford RA. 2012. Does waterproofing Thermochron iButton dataloggers influence temperature readings?. *Journal of Thermal Biology* **37**(4): 260–264.

Salerno F, Guyennon N, Thakuri S, Viviano G, Romano E, Vuillermoz E, Cristofanelli P, Stocchi P, Agrillo G, Ma Y, Tartari G. 2015. Weak precipitation, warm winters and springs impact glaciers of south slopes of Mt. Everest (central Himalaya) in the last 2 decades (1994–2013). *The Cryosphere* **9**: 1229–1247. https://doi.org/10.5194/tc-9-1229-201.

Sappington J, Longshore K, Thompson D. 2007. Quantifying landscape ruggedness for animal habitat analysis: a case study using bighorn sheep in the Mojave Desert. *Journal of Wildlife Management* **71**: 1419–1426.

Scherler D, Bookhagen B, Strecker MR. 2011. Spatially variable response of Himalayan glaciers to climate change affected by debris cover. *Nature Geoscience* **4**: 156–159. https://doi.org/10.1038/ngeo1068.

Shaw TE, Brock BW, Fyffe CL, Pellicciotti F, Rutter N, Diotri F. 2016. Air temperature distribution and energy-balance modelling of a debris-covered glacier. *Journal of Glaciology* **62**: 185–198. https://doi.org/10.1017/jog. 2016.31.

Shea JM, Immerzeel WW, Wagnon P, Vincent C, Bajracharya S. 2015. Modelling glacier change in the Everest region, Nepal Himalaya. *The Cryosphere* **9**: 1105–1128. https://doi.org/10.5194/tc-9-1105-2015.

Sherpa SF, Wagnon P, Brun F, Berthier E, Vincent C, Lejeune Y, Arnaud Y, Kayastha RB, Sinisalo A. 2017. Contrasted surface mass balances of debris-free glaciers observed between the southern and the inner parts of the Everest region (2007–2015). *Journal of Glaciology* **63**: 637–651.

Sicart JE, Pomeroy JW, Essery RLH, Bewley D. 2006. Incoming longwave radiation to melting snow: observations, sensitivity and estimation in Northern environments. *Hydrological Processes* **20**: 3697–3708. https://doi.org/10.1002/hyp. 6383.

Solano NA, Clarkson CR, Krause FF. 2016. Characterization of fine-scale rock structure and differences in mechanical properties in tight oil reservoirs: an evaluation at the scale of elementary lithological components combining photographic and X-ray computed tomographic imaging, profile-permeability and microhardness testing. *Journal of Unconventional Oil and Gas Resources* **15**: 22–42.

Steiner JF, Pellicciotti F. 2015. Variability of air temperature over a debris-covered glacier in the Nepalese Himalaya. *Annals of Glaciology* **57**: 295–307. https://doi.org/10.3189/2016AoG71A066.

Strasser U, Corripio J, Pellicciotti F, Burlando P, Brock B, Funk M. 2004. Spatial and temporal variability of meteorological variables at Haut Glacier d' Arolla (Switzerland) during the ablation season 2001: measurements and simulations. *Journal of Geophysical Research: Atmospheres* **109**. https://doi.org/10.1029/2003JD003973.

Suzuki R, Fujita K, Ageta Y. 2007. Spatial distribution of thermal properties on debris-covered glaciers in the Himalayas derived from ASTER data. *Bulletin of Glaciological Research* **24**: 13.

Swift DA, Nienow PW, Hoey TB, Mair DW. 2005. Seasonal evolution of runoff from Haut Glacier d'Arolla, Switzerland and implications for glacial geomorphic processes. *Journal of Hydrology* **309**(1): 133–148. https://doi.org/10.1016/j.jhydrol. 2004.11.016.

Takeuchi Y, Kayastha RB, Nakawo M. 2000. Characteristics of ablation and heat balance in debris-free and debris-covered areas on Khumbu Glacier, Nepal Himalayas, in the pre-monsoon season *in Debris-covered Glaciers: Proceedings of an international workshop held at the University of Washington. Seattle: Washington, USA* **264**: 53–62.

Van Den Broeke M, Reijmer C, Van As D, Boot W. 2006. Daily cycle of the surface energy balance in Antarctica and the influence of clouds. *International Journal of Climatology* **26**: 1587–1605. https://doi.org/10.1002/joc. 1323.

Vincent C, Wagnon P, Shea J, Immerzeel W, Kraaijenbrink P, Shrestha D, Sorunco A, Arnaud Y, Brun F, Berthier E, Sherpa S. 2016. Reduced melt on debris-covered glaciers: investigations from Changri Nup Glacier, Nepal. *The Cryosphere* **10**: 1845–1858.

Wagnon P, Ribstein P, Francou B, Pouyaud B. 1999. Annual cycle of energy balance of Zongo Glacier, Cordillera Real, Bolivia. *Journal of Geophysical Research: Atmospheres* **104**: 3907–3923. https://doi.org/10.1029/1998JD200011.

Watson CS, Quincey DJ, Carrivick JL, Smith MW. 2016. The dynamics of supraglacial ponds in the Everest region, central Himalaya. *Global and Planetary Change* **142**: 14–27.

Yasunari T. 1976. Seasonal weather variations in Khumbu Himal. *Journal of the Japanese Society of Snow and Ice* **38**: 74–83. https://doi.org/10.5331/seppyo. 38.Special_74.

Supporting Information

Additional supporting information may be found online in the Supporting Information section at the end of the article.

Figure S1: Temperature differences recorded by free and contained iButton sensors (black), and Tinytag sensors (grey), for (a) air, (b) water and (c) ice in laboratory conditions.
Appendix S1: Temperature sensor assessment.

